



Article

Satellite-Derived Shoreline Changes of an Urban Beach and Their Relationship to Coastal Engineering

Rijun Hu ^{1,2}, Yingjie Fan ¹ and Xiaodong Zhang ^{1,2,*}

¹ College of Marine Geosciences, Ocean University of China, Qingdao 266100, China; hrj@ouc.edu.cn (R.H.); fanyingjie@stu.ouc.edu.cn (Y.F.)

² Key Lab of Submarine Geosciences and Prospecting Techniques, Ministry of Education, Qingdao 266100, China

* Correspondence: zxd@ouc.edu.cn

Abstract: Urban beaches, oscillating between development and protection, are more frequently and strongly affected by human activities; therefore, comprehensive and detailed studies of the geomorphological evolution of urban beaches affected by coastal engineering are imperative. Based on 769 satellite images from 1986 to 2023, this study employed a transect-focused approach to investigate the historical shoreline change of Haikou Beach, an urban beach with three nearby offshore artificial islands. The satellite-derived mean water line positions have a temporal resolution of 41 days before 2014 and 9 days after 2018, with a random error of 4.9 m, ranking among the state-of-the-art in this field. This study revealed that the constructions of Pearl Island and Millennium Island as well as five beach nourishment projects mainly exerted a positive impact on the evolution of Haikou Beach. The beach in Pearl Island's wave shadow area may form a tombolo in a hundred years. In the context of heightened coastal engineering development, leveraging the existing large and future larger archives of satellite imagery to analyze the complex changes of urban beaches helps mitigate the absence of field data, aiding in the development of targeted beach erosion protection and remediation strategies with scientific, engineering, and societal significance.

Keywords: coastal engineering; offshore artificial island; sand replenishment; beach evolution; remote sensing



Citation: Hu, R.; Fan, Y.; Zhang, X. Satellite-Derived Shoreline Changes of an Urban Beach and Their Relationship to Coastal Engineering. *Remote Sens.* **2024**, *16*, 2469. <https://doi.org/10.3390/rs16132469>

Academic Editor: Andrea Storto

Received: 31 May 2024

Revised: 30 June 2024

Accepted: 2 July 2024

Published: 5 July 2024



Copyright: © 2024 by the authors. Licensee MDPI, Basel, Switzerland. This article is an open access article distributed under the terms and conditions of the Creative Commons Attribution (CC BY) license (<https://creativecommons.org/licenses/by/4.0/>).

1. Introduction

Beaches, situated in the transitional zone between land and sea, hold significant social, economic, and ecological value [1–3]. Due to decreased river sediment discharge, increasing sea levels, and heightened human activities, beaches commonly undergo continual and often detrimental changes [4–6]. Urban beaches, more closely associated with human activities, are consequently more affected by human interventions, including the construction of coastal engineering structures and beach nourishments.

The beach under study, Haikou Beach, is located adjacent to the central district of Haikou City, a metropolitan area with a population of 3 million. Multiple coastal engineering projects have been constructed around Haikou Beach, mainly as a result of urban development, as well as beach protection. These projects include three offshore artificial islands, five beach nourishment (also called sand replenishment) efforts, and five other coastal engineering structures. The construction of these projects, especially the offshore artificial islands, has changed the original near-natural shoreline evolution and landscape, which is the direct motivation for this study.

Field survey data are commonly used to study beach changes, revealing their responses to the influences mentioned above [7–9]. Previous studies on Haikou Beach, based on field surveys, have found mild erosion on the eastern part of the beach [10] and significant impacts from the construction of Pearl Island [11]. Accurate and reliable field survey data

are important for understanding beach evolution; however, due to resource and manpower constraints, long-term and continuous beach field survey data are limited to a small number of beaches (e.g., [2,8]). Like the vast majority of the world's beaches, Haikou Beach lacks long-term and continuous field survey data, which affects the in-depth understanding of shoreline changes and the assessment of coastal engineering impacts, especially those of offshore artificial islands.

To address the lack of field data, current researchers have mainly utilized long-term, continuous, and publicly available satellite imagery, such as Landsat and Sentinel, to study the long-term evolution of beaches [12–16]. However, the use of Landsat and Sentinel images to study beach evolution is affected by various factors, such as clouds, waves, water transparency, water level fluctuations, and beach morphology, in addition to their relatively coarse spatial resolution (10–30 m) [17–28]. Researchers have employed a variety of techniques and approaches to address these challenges. Pardo-Pascual et al. [17–19] utilized subpixel shoreline identification technology to extract the waterline of the steep Spanish coast; the subpixel technology overcame the limitations of Landsat images in spatial resolution, and the random error of the shoreline position was reduced to 4.7–6.6 m. Hagenaaers et al. [20] used a 1D Gaussian smoothing operation to obtain a gradual shoreline, and the accuracy of the satellite-derived shoreline position was determined with subpixel precision. Vos et al. [21,22] shared a software for recognizing shorelines on satellite images based on subpixel technology, and the random errors of the shoreline position interpreted from four typical beaches with slopes ranging from 1:25 to 1:9 were 6.9–48.3 m; additionally, the beach with a gentler slope had better shoreline position accuracy. Castelle et al. [23] used the program shared by Vos et al. [19] to recognize the shorelines of Truc Vert Beach with slopes ranging from 1:9 to 1:50, and the random position errors of the shorelines were 6.0–14.1 m.

Zhang et al. [24–29] utilized a transect-focused approach and shared a software for recognizing shoreline positions on transects based on subpixel technology; the software combined automatic and interactive identification methods to obtain as many shoreline positions as possible from satellite imagery to improve the accuracy and reliability of shoreline positions, and the random errors of the shoreline positions were 3.9–6.5 m and 8.4–15.9 m for steep and gentle beach, respectively. In summary, the adoption of subpixel technology has significantly improved the accuracy of shoreline position identification, with the current best accuracy of satellite-derived shoreline positions being about 4–7 m, which are mainly derived from beaches with steep slope (e.g., [19,22,28]). The use of a large number of satellite images has not only improved the temporal resolution of the study, but has also further increased the accuracy of the results through statistical methods [28].

Regarding the impact of offshore artificial islands on beach evolution, this type of research is still in a preliminary stage. The studies conducted by Zhang et al. [25,28] on Lianli Island and Xingguang Island show that the construction of the two large offshore artificial islands has resulted in rapid accretion of their sheltered beaches; however, these sheltered beaches happen to have estuaries, and the highly dynamic character of estuaries and frequent estuarine regulation projects limit the understanding of the impact of the artificial islands. Based on four Landsat images, Subraelu et al. [30] utilized four Landsat images to reveal the shoreline changes adjacent to the offshore artificial islands in the United Arab Emirates, and found the shoreline experienced a notable shoreline retreat with an erosion rate of 30 m/year during 2000–2021. It is worth noting that the results derived from limited number of satellite images have shortcomings in terms of temporal resolution.

Primarily based on topographic data, Li et al. [6] studied the effects of offshore artificial islands in Hongtang Bay on the stability of adjacent beaches, and the results indicate that the offshore artificial island with a large offshore distance and a small area has relatively small adverse effects. Related studies also include the Pearl Island study by Liu et al. [11] based on field survey data, which was just mentioned and will be compared in detail with our findings in the discussion. These field-surveyed topographic and shoreline position data also suffer from insufficient quantity, which limits the level of detail of the findings.

Research on the evolution of urban beaches based on satellite images has made great progress, but (1) the spatiotemporal scope and resolution of the research results still need to be improved, and (2) the impact and the impact mechanisms of offshore artificial islands on their nearby beaches are still poorly understood. This paper uses 769 Landsat and Sentinel images from 1986 to 2023 to study the spatiotemporal evolution of Haikou Beach, aiming to (1) show the detailed change process and link the changes to the construction of coastal engineering projects, including three offshore artificial islands; (2) reveal the impact mechanisms, providing recommendations and references for the protection and restoration of Haikou Beach; and (3) provide a new method for environmental impact assessment of coastal engineering, especially of offshore artificial islands, based on freely available satellite imagery.

2. Study Area

Haikou Beach is situated in Haikou City, the capital of Hainan Province, China. It spans 21 km along the coast, comprising four small pocket beaches on the west side and a longer, straight beach on the east side (Figure 1). Hainan Province, located at the southernmost point of China, is the newest and largest special economic zone in the country. To the south of Haikou Beach lies the bustling downtown area of Haikou City, with a coastal park ranging from 20 to 110 m in width adjacent to the beach, followed by city roads and buildings further south. The sediment on Haikou Beach consists mainly of sand (97% on average), with a median grain size ranging from 0.14 to 3.68 mm (0.31 mm on average) [10]; and the intertidal zone of Haikou Beach is steep, with an averaged slope of 1:10 [10,11].

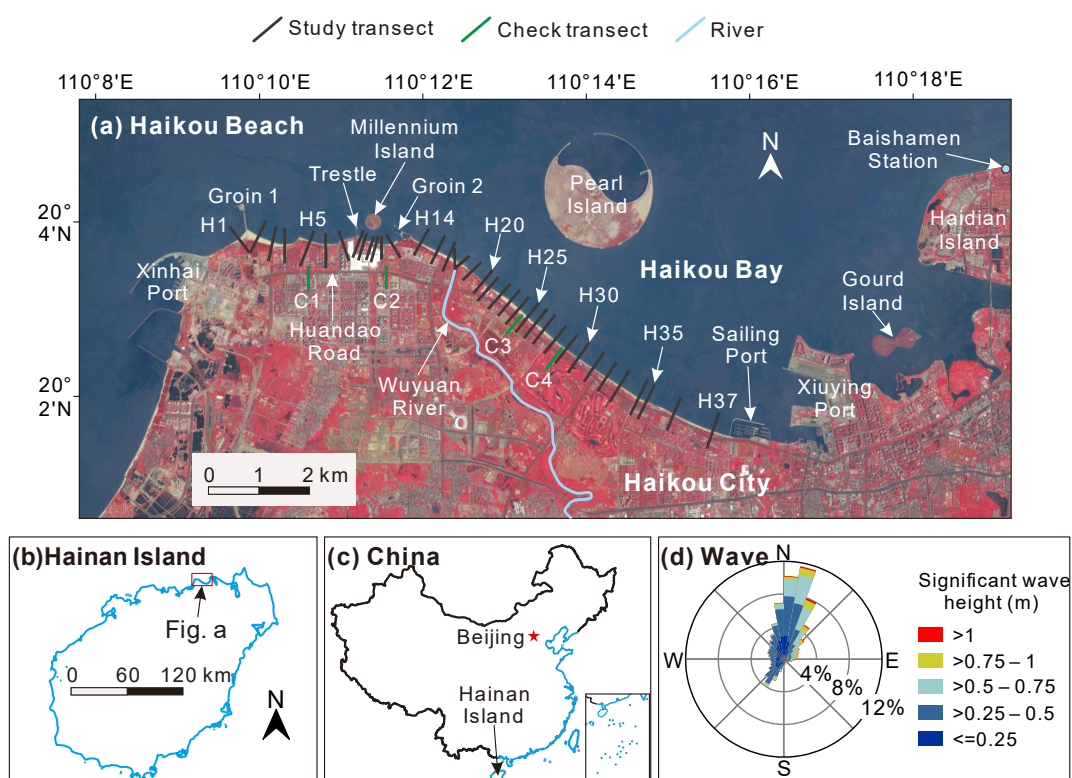


Figure 1. Haikou Beach (a) and its location on Hainan Island (b), China (c); and (d) the significant wave heights of study area. The background for Figure 1a is the mean image of all the cloud-free Sentinel-2 images acquired in 2021–2022.

Three offshore artificial islands—Pearl Island, Millennium Island, and Gourd Island—are situated in close proximity to Haikou Beach, along with five coastal hard structures including Groin 1, Trestle, Groin 2, Sailing Port, and Xiuying Port (Figures 1, A1 and A2). Among the three offshore artificial islands, Pearl Island is the largest, with a diameter of

2.3 km, a closest offshore distance of 1.85 km, a sea area of 4.3 km², and a land area of 2.5 km², with a standard circular shape (Figure 1). Millennium Island is the smallest, with a diameter of 0.34 km, a closest offshore distance of 0.25 km, and a land area of 0.09 km², with a standard solid circular shape (Figures 1 and A1). Gourd Island is of medium size, measuring 1 km in length, 0.5 km in width, with a closest offshore distance of 0.42 km, and a land area of 0.31 km², resembling a gourd (Figures 1 and A2). Additionally, five beach nourishment projects have been executed near Pearl Island and Millennium Island (Figures A3 and A4), with a total of 1.54 million m³ of sand replenished [31].

Based on wave observation data from the Baishamen Hydrological Station (located 7 km northeast of Haikou Beach, refer to Figure 1a), the waves in the study area primarily consist of wind waves, with a probability of occurrence ranging from 77% to 86%. The predominant directions for significant and strong waves are from the north-northeast (NNE), followed by northeast (NE) and north (N) (Figure 1d), and the averaged significant wave height is 0.6 m, with a maximum wave height of 3.5 m [11,32]. The tidal regime in the study area is characterized as irregular diurnal tides with a small tidal range, averaging 1.11 m, and the mean high and low water levels are 0.52 and −0.58 m, respectively, relative to mean sea level.

The Wuyuan River flows into the sea in the middle of the beach. This small river, with a total length of 29 km and a drainage area of 85 km², has limited sediment supply. Instead, the sediment discharged by the Nanduijiang River, located 10 km east of Haikou Beach, is considered the primary sediment source for the study area [11,32]. The Nanduijiang River is the largest river on Hainan Island, with a total length of 341 km, a drainage area of 7033 km², and an average annual runoff of 68 billion m³ [10,11]. However, mainly due to dam construction in the 1970s, the sediment discharge from the Nanduijiang River into the sea has significantly decreased from 680 k ton/year in the 1950s to 150 k ton/year in the 2000s. The embankment projects at the mouth of the Nanduijiang River occupied shallow seas, thereby impeding fluvial sediment transport; consequently, there was hardly any fluvial sediment from the river that could be transported to Haikou Bay after 2000 [10,11].

3. Data and Methods

3.1. Data Source and Preprocessing of Satellite Images

The satellite images used in this study were obtained from the Google Earth Engine (<https://earthengine.google.com/>, accessed on 1 January 2024; e.g., [33]) using the GEE downloader, a JavaScript program (<https://github.com/oucxd/CASPRS>, accessed on 1 January 2024, e.g., [29]). The program allows the users to selectively download satellite images in batches by setting the image areas to be downloaded and setting parameters such as bands, cloud cover, date, and image types, which improves efficiency.

The cloud cover of the downloaded satellite images was set to less than 80%. The satellite image types included Landsat TM, ETM+, and OLI (30 m resolution) as well as Sentinel-2 MSI (10 m resolution). After manually eliminating images where more than half of the shoreline was obscured by factors such as clouds, cloud shadows, sea fog, and sensor malfunctions, 554 Landsat and 215 Sentinel images remained, totaling 769 images.

The time range of the satellite images extended from 1986 to 2023, averaging 20 images per year. The images before 2014 are relatively few, averaging 12 images per year. Following the successive launch of the Sentinel-2 A and B satellites after 2015, the number of available satellite images gradually increased to an average of 54 images per year after 2018 (Figure 2a,b). The standard false-color method (using the near-infrared, red, and green bands as the red, green, and blue components of the composite image) was used to synthesize the satellite images, resulting in significant color differences between sand and seawater on the composite image (Figures 1 and 3). In summary, all available Landsat (30 m resolution) and Sentinel-2 (10 m resolution) images of the study area were downloaded, and the same synthesis method and a consistent spatial resolution of 10 m were used to ensure comparable image results.

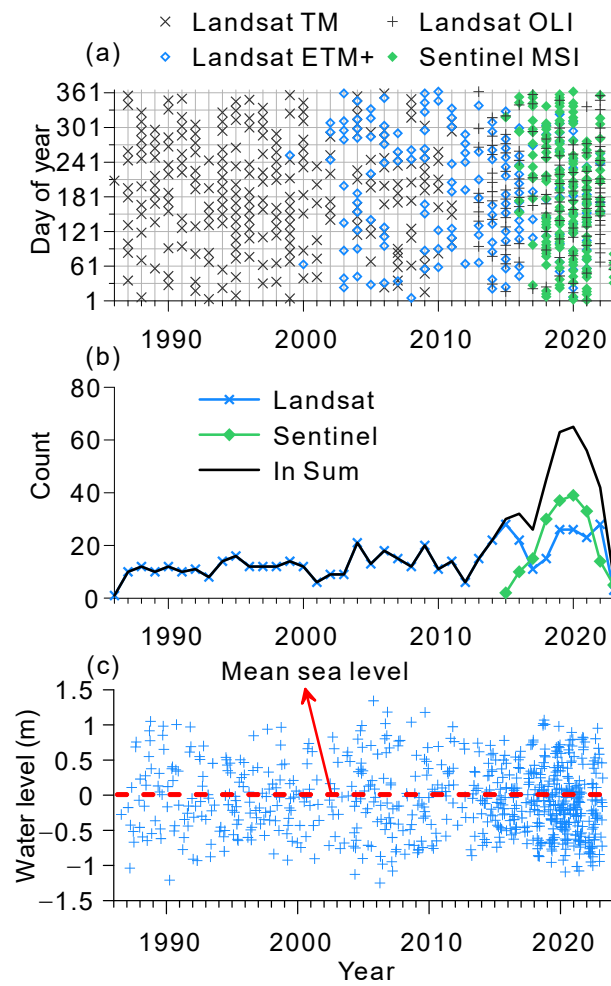


Figure 2. Acquisition dates, sensor types (a), annual counts (b), and instantaneous water levels (c) of the Landsat and Sentinel satellite images of Haikou Beach from 1986 to 2023.

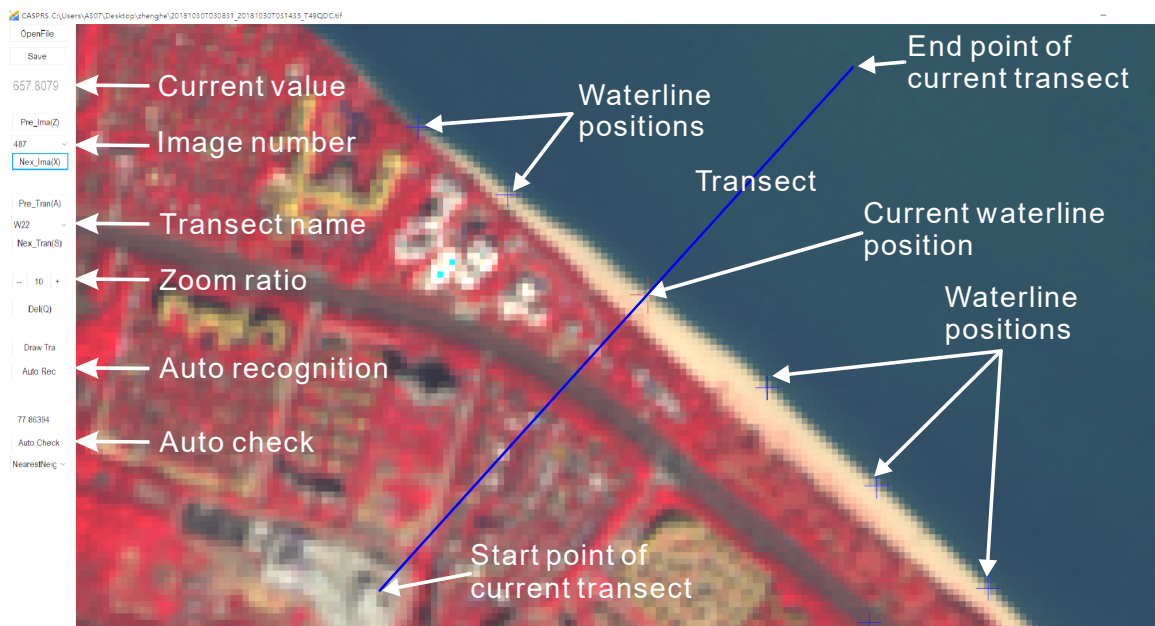


Figure 3. Recognition of waterline positions using transect-focused computer-aided shoreline position recognition software (CASPRS).

3.2. Historical Water Heights

The historical water levels were simulated using the regional ocean tide model NAO.99Jb [34], and the simulated water levels were corrected by the seasonal sea-level bias of the Xiuying Port [24,28]. The water levels when the satellite images were captured mainly ranged between -1.25 and 1.29 m (Figure 2c).

3.3. Recognition of Shoreline Positions on Transects

According to the spatial distribution of the coastal engineering projects, thirty-seven study transects were set up along the shoreline at 100–900 m intervals to investigate the historical shoreline changes of Haikou Beach. The study transects were primarily established based on the complexity of the local shorelines and the neighboring coastal engineering. Fewer study transects were set up for straight shorelines, while more transects were set up for curved and complex shorelines. Additionally, the study transects were placed flexibly, considering the importance and characteristics of the coastal engineering features. For example, a total of 18 study transects were set up from H19–30 along the shoreline directly opposite Pearl Island, which is the focus of this paper.

The transect-focused computer-aided shoreline position recognition software (CASPRS ver 2.1) [29] was used to identify the waterline positions on these transects (Figure 3). CASPRS employs subpixel recognition technology and a combination of automatic and interactive methods to directly identify the shoreline positions on the transects, making it suitable for processing a large number of satellite images [24–28].

The CASPRS project consists of two files with the suffixes “CAS” and “CSV”, which must have the same name. Currently, these two files need to be created manually based on the samples. After opening the CAS file, the recognition process begins, and the recognition results are then saved in the CSV file for further processing and analysis. The recognition process was divided into three steps. Firstly, click the “Auto Rec” button to perform automatic recognition, then click the “Auto Check” button to carry out automatic check of the automatic recognition results. Finally, click the “Pre_Ima”, “Next_Ima”, “Pre_Tran”, and “Next_Tran” buttons to switch between all the images and transects, proofreading them one by one.

After the automatic and manual operations, a total of 21,003 shoreline positions on the 37 transects of the 769 images were obtained, resulting in a data acquisition rate of 74%. Considering the annual numbers of satellite images, the temporal resolution of the satellite-derived shoreline positions at Haikou Beach was averaged at 41 days before 2014 and 9 days after 2018.

3.4. Geographical Correction, Water Level Correction, and Error Assessment

Huandao Road, 32 m wide and parallel to the shoreline, was used to assess the geographical positioning errors of the Landsat and Sentinel images, referring to Zhang et al. (2024) [28]. Four check transects (C1–4) were set perpendicular to this road (Figure 1), and the positions of the centerline of this road on transects C1–4 were used to evaluate and correct the geographical positioning errors of the Landsat and Sentinel images in the north–south direction (C1–2) and the northeast–southwest direction (C3–4), which are the main directions of these study transects.

The water level correction method was used to adjust the waterline positions to mean sea levels using the previously mentioned simulated water levels and the intertidal slopes, which were estimated using the simulated water levels and waterline positions, referring to Zhang et al. (2021, 2024) [25,28]. The corrected shoreline positions were termed as mean water line positions and were further averaged annually to obtain the annual mean water line positions. The random errors of the waterline positions and the mean water line

positions were assessed using Equation (1) referring to Zhang et al. (2021, 2024) [25,28], since the beach studied lacked long-term and continuous field-surveyed data.

$$E_{sp} = \sqrt{\frac{1}{n-1} \sum_{i=1}^n (SP_i - \overline{SP}_y)^2} \quad (1)$$

where E_{sp} is the random error of shoreline positions, n is the total number of the shoreline positions, SP_i is the i -th shoreline position, and \overline{SP}_y is the annual mean shoreline position for the year of the i -th shoreline position. The physical meaning of the error is the standard deviation of these shoreline positions after removing long-term trends.

4. Results

4.1. Construction Process of Major Coastal Engineering

The commencement and completion dates of the major coastal engineering projects around Haikou Beach since 1986 (Table 1) have been predominantly ascertained through the analysis of 769 satellite images. Figure 4 illustrates the construction process of Pearl Island, while Figures A1 and A2 display the construction processes of coastal engineering in the western and eastern parts of the beach, respectively. Additionally, Figures A3 and A4 illustrate five beach nourishment processes.

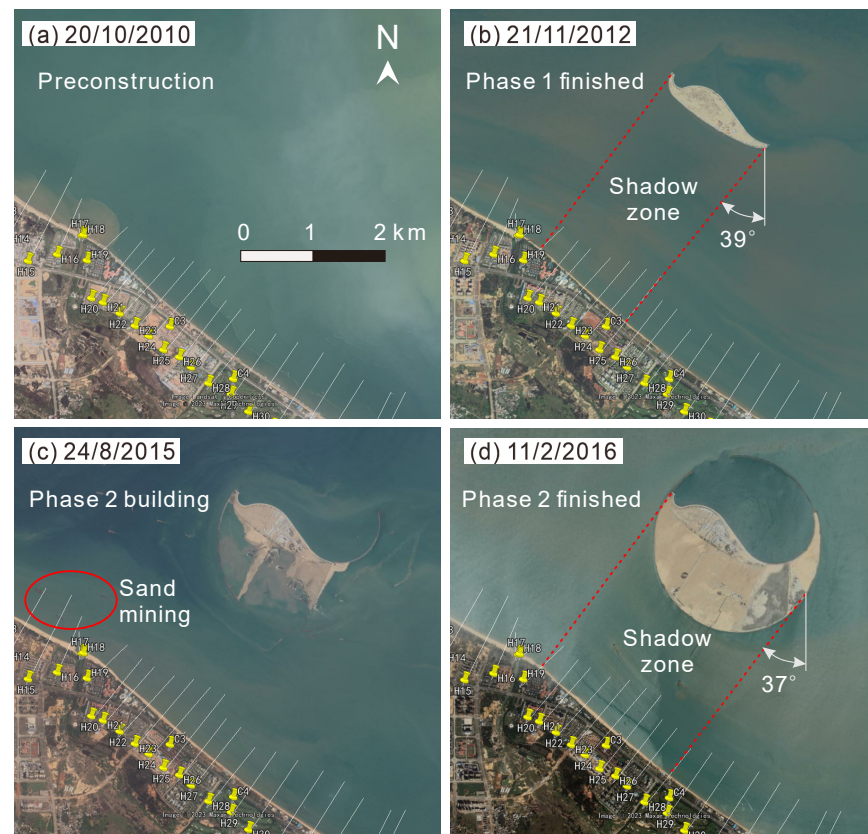


Figure 4. Building process of Pearl Island: (a) Preconstruction, (b) Phase 1 finished, (c) Phase 2 building, and (d) Phase 2 finished. Background images are from Google Earth.

Pearl Island was constructed in two phases: the core area was built from 2011 to 2012, and the outer area was constructed from 2015 to 2016 (Figure 4). Construction of Millennium Island began in 2013 and was completed in the same year (Figure A1). Gourd Island was constructed from 2009 to 2010 but was dismantled in 2021 (Figure A2).

Xiuying Port is the oldest and most important port in Hainan, established in 1936 and continuously expanded until reaching its maximum size in 2008. The remaining coastal hard structures were relatively small in scale and were completed within one year (Table 1,

Figures A1 and A2). Five beach nourishment events occurred near Millennium Island and Pearl Island (Table 1, Figures A3 and A4). Nourishments 1–2 near Millennium Island began in 2021–2022 and were completed within 1–2 months. Nourishments 3–5 near Pearl Island started in 2022 and took 2–4 months to complete.

Table 1. Major coastal engineering projects at Haikou Beach constructed after 1986. The starting date refers to the date of the earliest satellite image displaying the project, while the finishing date refers to the date of the earliest satellite image showing the complete outline of the project. Considering the time intervals of satellite images in the study area, the accuracy of these dates is approximately 41 days before 2018 and 9 days after 2018.

| Name | Location | Starting Date | Finishing Date |
|----------------------|---------------------------|------------------|------------------|
| Groin 1 | Between H1 and H2 | 17 January 2015 | 17 January 2015 |
| Trestle | Between H7 and H8 | 31 May 2000 | 7 November 2000 |
| Millennium Island | Next to H8–13 | 8 March 2013 | 26 October 2013 |
| Groin 2 | Between H13 and H14 | 12 March 2008 | 22 June 2008 |
| Pearl Island Phase 1 | Next to H19–25 | 26 August 2011 | 11 July 2012 |
| Pearl Island Phase 2 | Next to H19–29 | 12 July 2015 | 11 February 2016 |
| Sailing Port | East of H37 | 3 April 2018 | 23 January 2019 |
| Xiuying Port | Northeast of Sailing Port | 1936 * | 2 March 2008 |
| Gourd Island | Northeast of Xiuying Port | 27 July 2009 | 3 December 2010 |
| Nourishment 1 | Next to H6 | 20 May 2022 | 15 July 2022 |
| Nourishment 2 | Next to H7–8 | 13 March 2021 | 12 April 2021 |
| Nourishment 3 | Next to H9–13 | 11 February 2022 | 22 April 2022 |
| Nourishment 4 | Next to H19–22 | 11 February 2022 | 20 May 2022 |
| Nourishment 5 | Next to H26–34 | 2 January 2022 | 6 June 2022 |

* from historical documents.

4.2. Error Assessment Results

Figure 5 illustrates the Landsat- and Sentinel-derived positions of Huandao Road on check transects C1–4. Their mean positions show close agreement, with deviations ranging from 0.6 to 4.3 m. The random position error on Landsat images ranges from 1.5 to 3.3 m, while on Sentinel images it ranges from 4.2 to 5.0 m, indicating larger error on Sentinel images (Table 2). Further analysis reveals a strong positive correlation in the Sentinel-derived positions, whereas the Landsat-derived positions show little correlation (Figure 6). These results indicate that the geographical position of the Sentinel-2 images requires correction, while the Landsat images do not require further correction. The Sentinel-derived positions of Huandao Road on C1–4 were used to perform the geographical position correction to Sentinel images. In addition, the nearly synchronous position changes of Huandao Road on transects C1–4 also indicate that rotation correction is not required for either Landsat or Sentinel images.

Table 2. Satellite-derived positions of Huandao Road on check transects C1–4 and their systematic and random errors. All data are in meters.

| | C1 | C2 | C3 | C4 |
|--|-------|-------|-------|-------|
| Mean position on Sentinel images | 135.3 | 199.2 | 180.4 | 201.0 |
| Mean position on Landsat images | 132.1 | 194.9 | 178.8 | 200.3 |
| Systematic position error | 3.2 | 4.3 | 1.6 | 0.6 |
| Random position error on Sentinel images | 5.0 | 4.5 | 4.2 | 4.3 |
| Random position error on Landsat images | 1.5 | 2.2 | 3.3 | 3.2 |

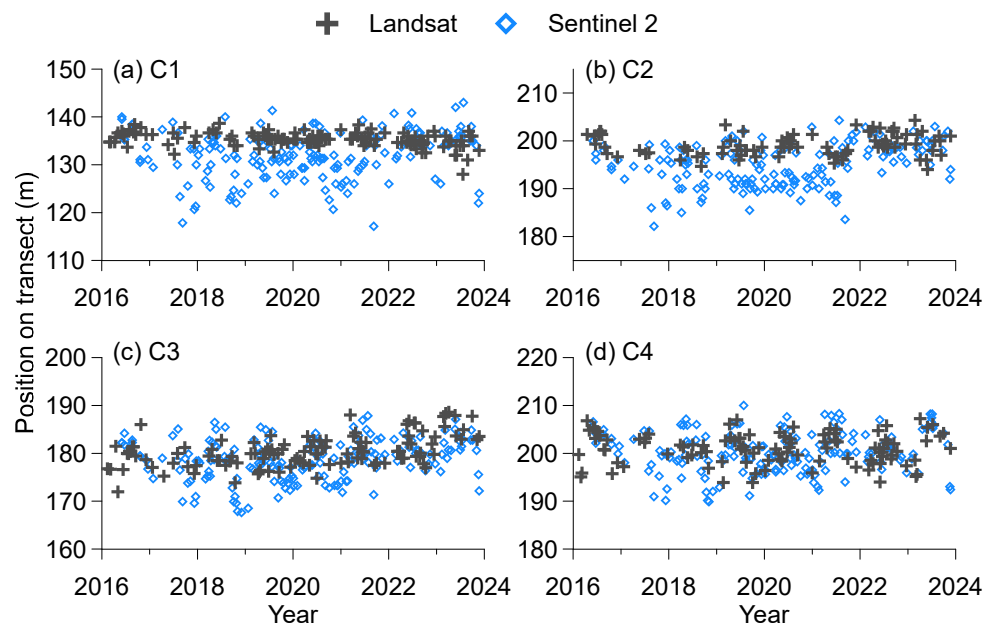


Figure 5. Landsat- and Sentinel-derived positions of Huandao Road on check transects C1–4 (a–d).

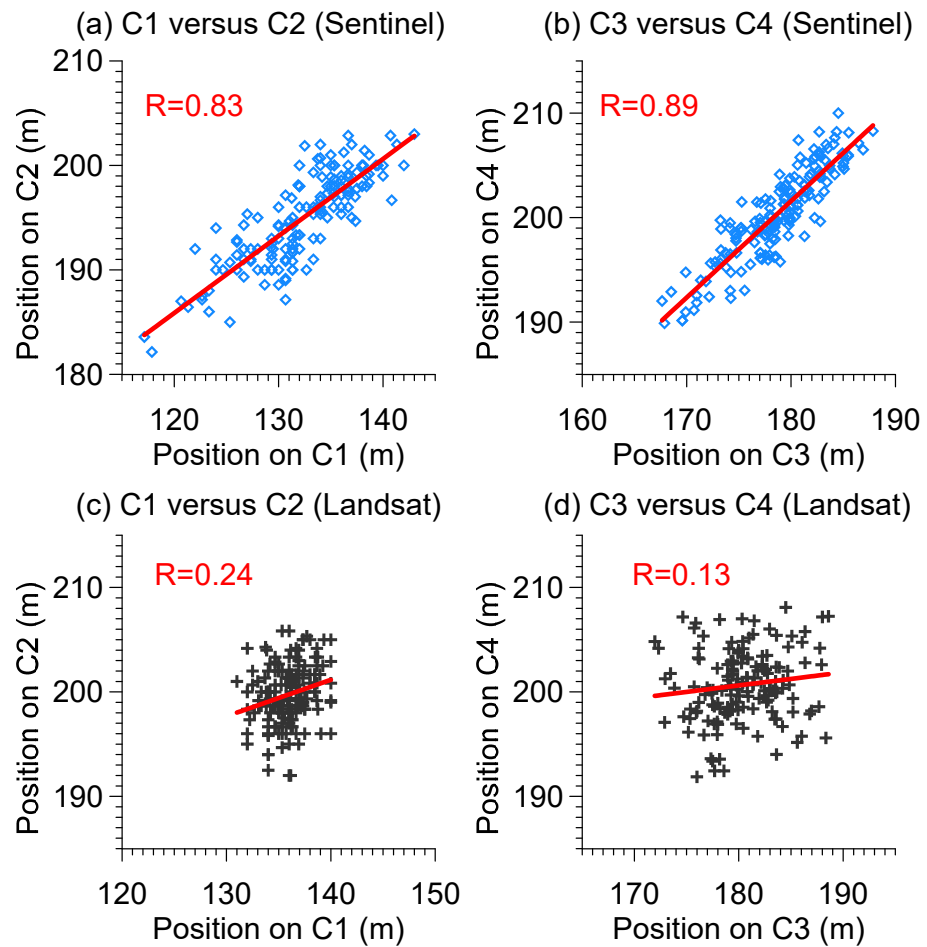


Figure 6. Scatterplots between the Sentinel-derived positions of Huandao Road on check transects C1–2 (a) and C3–4 (b), and the scatterplots between the Landsat-derived positions of Huandao Road on check transects C1–2 (c) and C3–4 (d).

In addition to the geographical correction, water level correction was also applied to the waterline positions. After these corrections, the mean random error of the satellite-derived shoreline positions on H1–37 decreased from 8.4 to 5.4 m (Figure 7). Compared to other transects, transects H16–18 exhibit larger random errors, attributed to their proximity to the Wuyuan River estuary, where the shoreline position change is significantly impacted by estuarine geomorphology such as river channels and sandbars [25–27]. Excluding these three transects, the mean random error of the satellite-derived shoreline positions on H1–15 and H19–37 decreased from 7.9 m before correction to 4.9 m after correction. The random errors in the corrected shoreline positions at Haikou Beach rank among state-of-the-art studies (e.g., [17–28]).

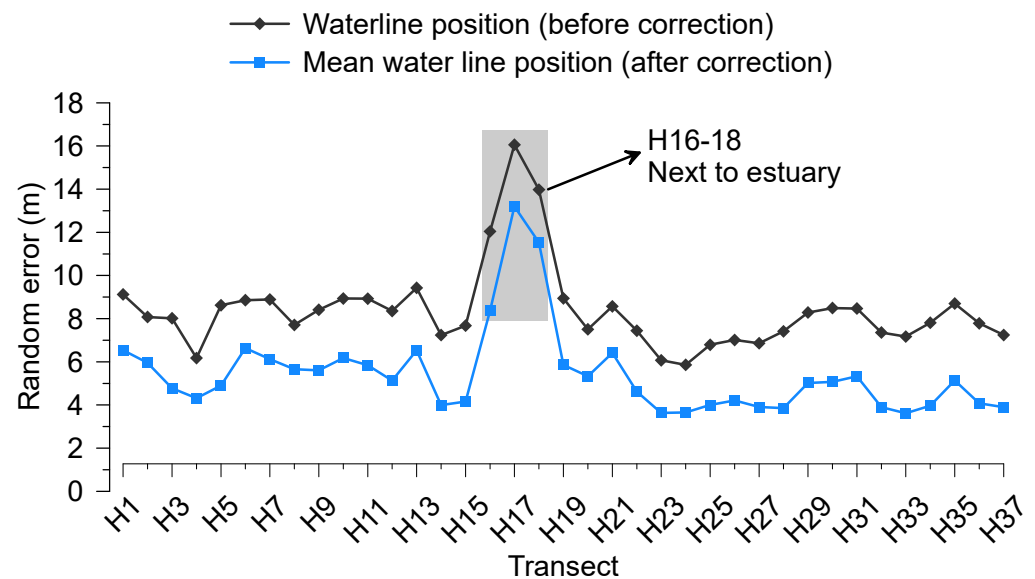


Figure 7. Random errors of the shoreline positions of Haikou beaches.

4.3. Shoreline Changes on 37 Transects

Figures 8–10 illustrate the satellite-derived mean water line positions on transects H1–37 from 1986 to 2023. The shoreline changes show diverse patterns along the beach, including initial accretion followed by accelerated accretion, transition from accretion to stability, shift from stability to erosion, rapid accretion due to sand replenishment, and patterns of erosion, accretion, and erosion.

Transects H1–3 experienced initial accretion, followed by accelerated accretion. Transect H4 transitioned from accretion to stability. Transects H5–6 shifted from stability to erosion, with rapid accretion in 2022 due to sand replenishment. Transect H7 initially accreted, then eroded, and experienced rapid accretion due to sand replenishment in 2021, followed by erosion. H8–12 exhibited erosion, accelerated erosion, stability, and sudden rapid accretion due to sand replenishment. H14–15 displayed a pattern of erosion, accretion, and erosion.

The short-term (less than 1 year) fluctuations in the mean water line position on transects H16–18 were significant, generally exceeding 50 m and reaching up to 150 m, unlike other transects where short-term fluctuations typically did not exceed 20 m. This is attributed to the influence of estuarine geomorphology, as shown before. Despite the significant short-term fluctuations, their long-term changes remained relatively stable.

Transects H19–28 initially showed minor erosion, transitioning to accretion after 2011. Among these, H19–22 shifted from accretion to erosion after 2015, with a reversion to accretion in 2019–2020. H19–22 and H26–28 experienced rapid accretion followed by rapid erosion in 2022 due to beach nourishments. H29–30 initially exhibited minor erosion, rapidly accreted due to beach nourishment in 2022, followed by rapid erosion. H31–33 initially eroded, shifted to accretion in 1996, and subsequently reverted to erosion after

2012, with rapid accretion followed by rapid erosion in 2022 due to beach nourishment. H34–37 initially experienced minor accretion, turned to rapid erosion in 2015, and shifted to minor accretion or erosion in 2017–2018.

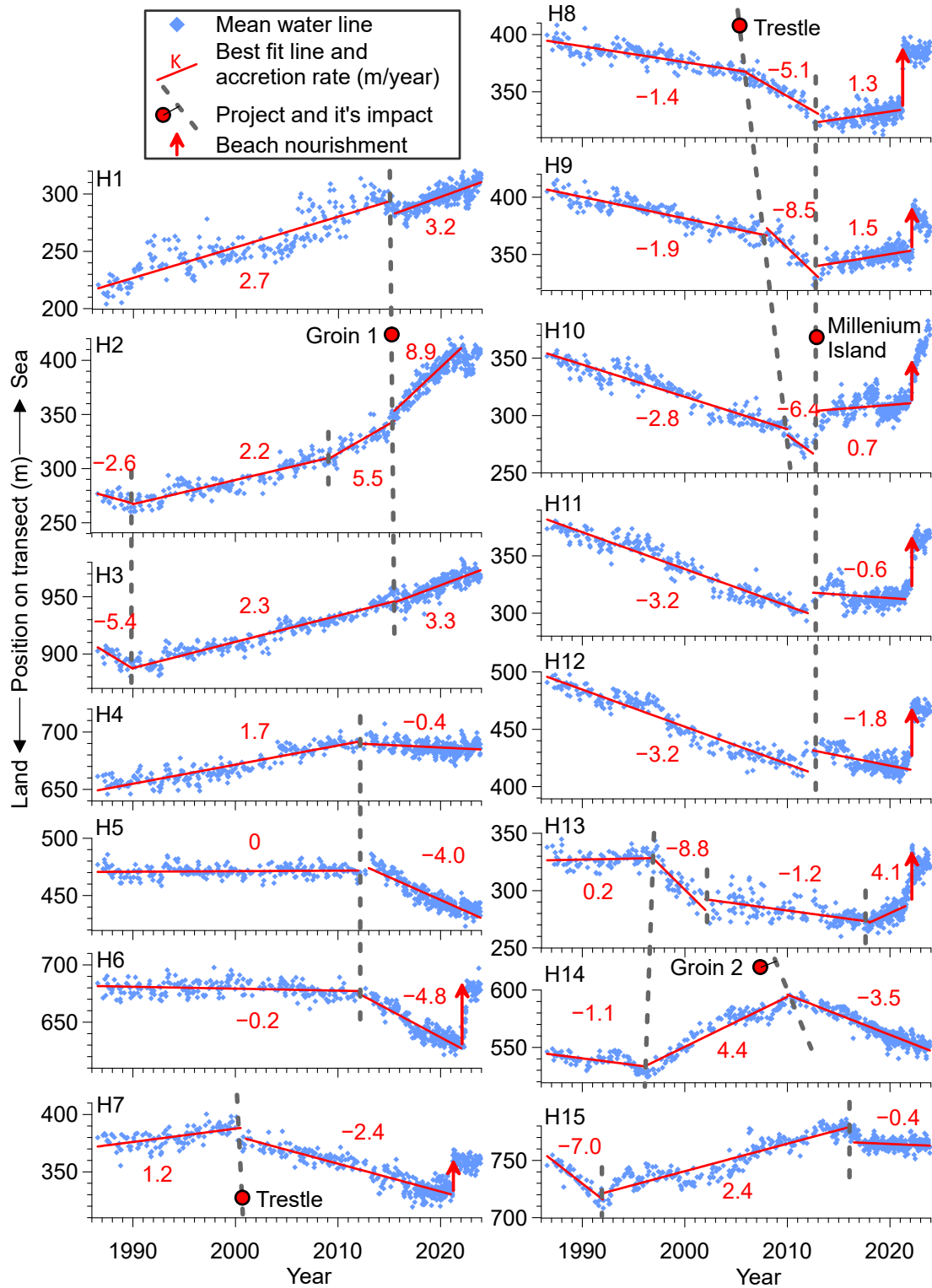


Figure 8. Satellite-derived mean water line positions on transects H1–15 from 1986 to 2023.

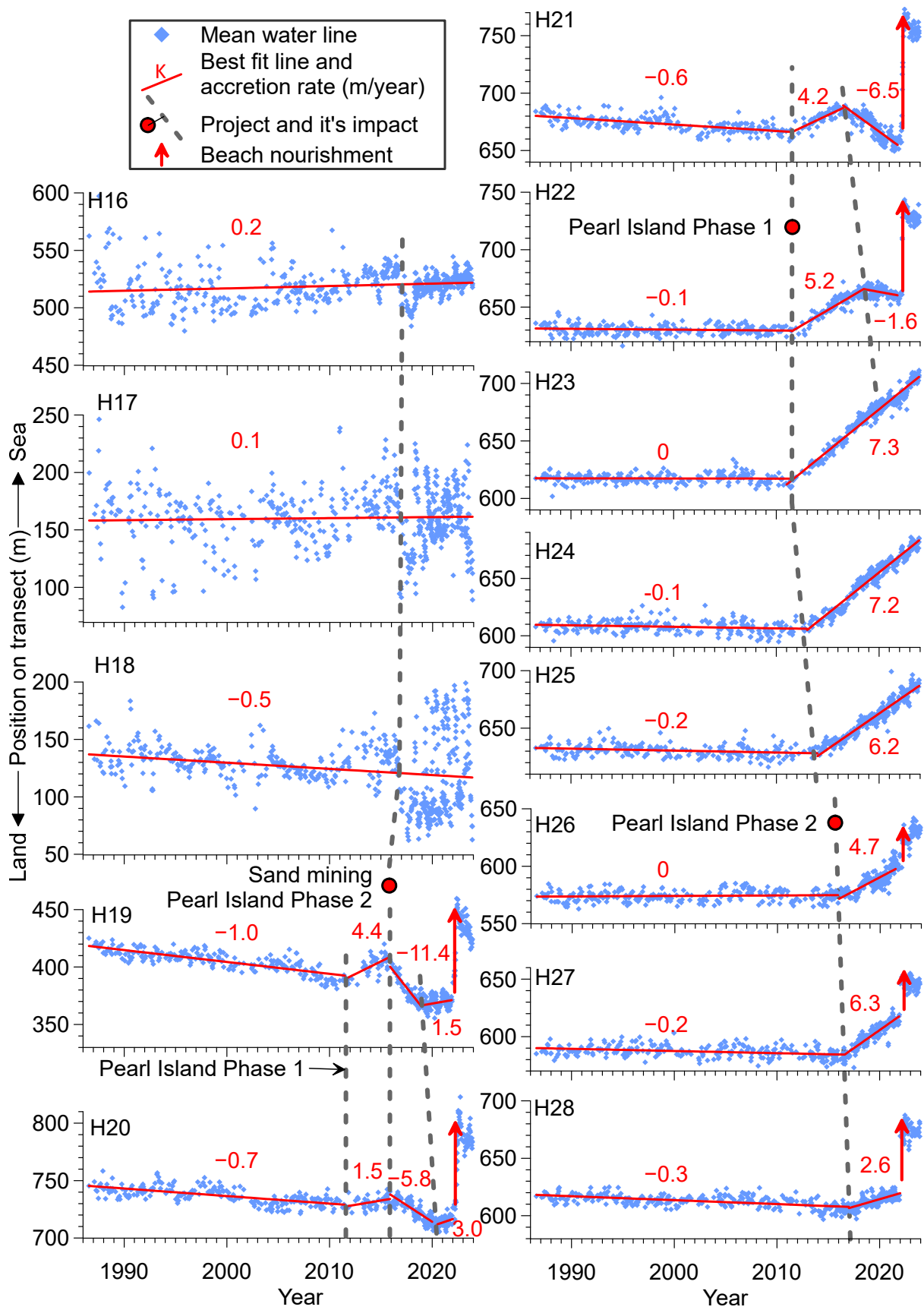


Figure 9. Satellite-derived mean water line positions on transects H16–28 from 1986 to 2023.

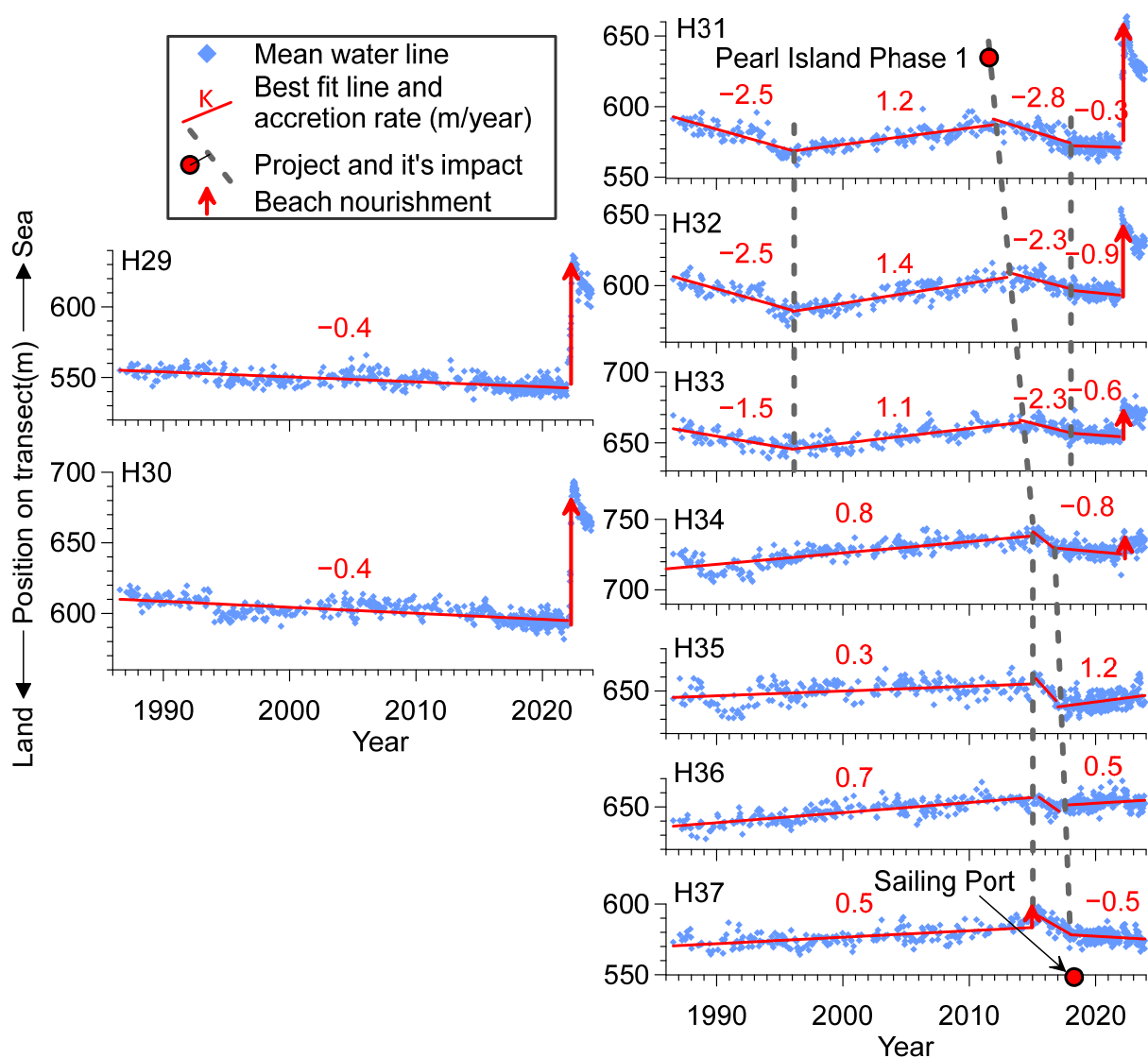


Figure 10. Satellite-derived mean water line positions on transects H29–37 from 1986 to 2023.

4.4. Shoreline Changes during Key Periods

The shoreline changes of Haikou Beach can be divided into three periods: early (1986–2010), middle (2010–2020), and late (2020–2023). The early period represents a time when coastal engineering was not extensively constructed, and the beach underwent relatively mild changes. The middle period signifies the extensive construction of coastal engineering, which significantly impacted the beach. The late period indicates the overwhelming impact of the beach nourishment projects (Figure 11).

Due to the limited annual number of satellite images in the early period, this study used the average shoreline positions from 54 satellite images during 1987–1991 to represent the shoreline position in 1989, indicating the starting point of the early period. Similarly, the average shoreline positions from 45 satellite images during 2009–2011 were used to represent the shoreline position in 2010, indicating the end of the early period and the beginning of the middle period. The annual number of satellite images in 2020 and 2023 was relatively high, with 65 and 40 images respectively, so their annual averages were directly used. Figures 11 and A5 illustrate the shoreline change rates and shoreline movements of Haikou beaches during the three periods.

During 1989–2010 (early period), most transects exhibited small shoreline change rates, but due to the long period, the shoreline movements were still considerable. Transects

H1–4 and H14–15 in the west experienced accretion, while transects H6–13 between them showed erosion, with approximately equal maximum accretion and erosion distances of about 60 m. Transects H18–30 in the east eroded, while the further east H31–37 accreted, with approximately equal maximum accretion and erosion distances of about 20 m.

During 2010–2020 (middle period), the transects H10–11 and H22–28 shifted from erosion to accretion, while the transects H14–15 and H31–37 shifted from accretion to erosion. The accretion rate was relatively high, but due to the shorter period, the accretion distance was comparable to the previous period.

During 2020–2023 (late period), the beach showed overwhelming accretion. Transects H6–13, H19–22, and H26–32 experienced significant shoreline accretion, with a maximum shoreline accretion rate of 30 m/year and a maximum accretion distance of 93 m.

Overall, transects H1–4 in the west and transects H19–37 in the east experienced accretion, with a maximum accretion distance of 136 m; while transects H5–18 showed an interplay of accretion and erosion, with a slight dominance of erosion and a maximum erosion distance of 33 m.

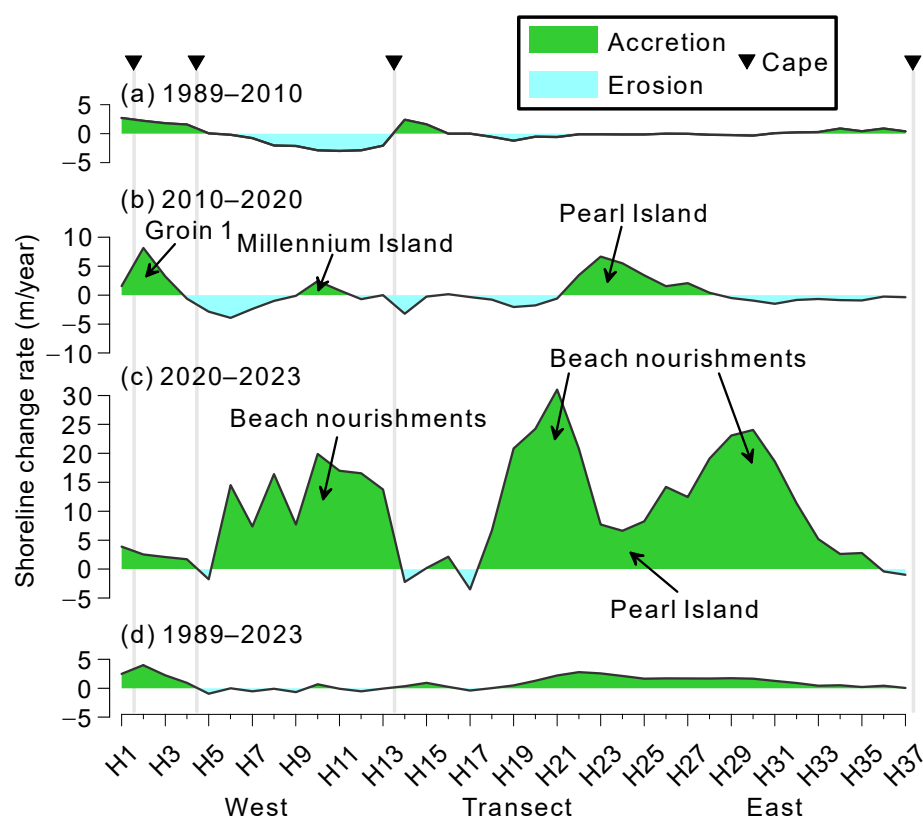


Figure 11. Shoreline change rates of Haikou beach during 1989–2010 (a), 2010–2020 (b), 2020–2023 (c), and 1989–2023 (d).

4.5. Shoreline Changes before and after the Construction of Pearl Island

Before the construction of Pearl Island (2001–2011), the western transects experienced weak erosion, while the eastern transects experienced weak accretion. After the completion of Pearl Island Phase 1 but before Phase 2 began construction (2011–2015), the previous western erosion and eastern accretion pattern reversed (Figures 12b and A6b). Transects H19–23 immediately accreted after the construction of Pearl Island Phase 1, with neighboring H24–25 beginning to accrete 1–2 years later. Transects H23–24 experienced a relatively high accretion rate, which decreased towards both sides (Figure 9). Transects H31–33 shifted from accretion to erosion within 1–3 years after the construction of Pearl Island Phase 1 (Figure 10).

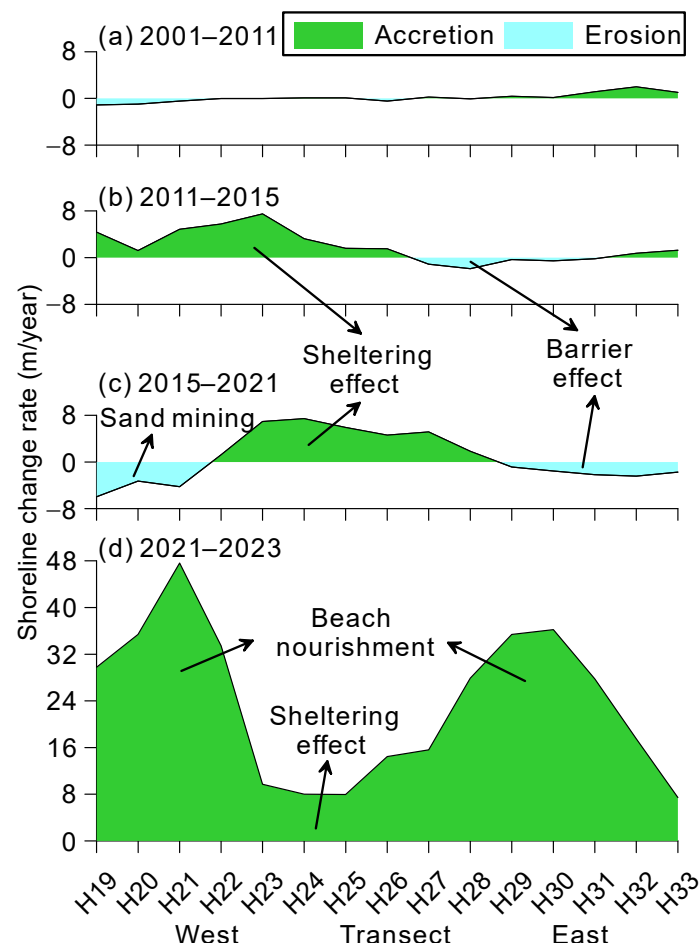


Figure 12. Shoreline change rates of Haikou beach next to Pearl Island during 2001–2011 (a), 2011–2015 (b), 2015–2021 (c), and 2021–2023 (d).

After the completion of Pearl Island Phase 2 but before the beach nourishment projects (2015–2021), transects H22–28 experienced accretion, while the remaining transects experienced erosion (Figures 12c and A6c). Transects H19–20 immediately transitioned from accretion to erosion after the construction of Pearl Island Phase 2, and their neighboring transects H21–22 followed suit in 2016–2017. The erosion on H19–20 lasted 3–4 years, while the erosion on transects H21–22 continued until it was interrupted by the beach nourishment in 2022. Transects H26–28 transitioned from stability to accretion in 2015–2016, with slightly lower accretion rates than their western counterparts, transects H23–25 (Figure 9).

After the implementation of beach nourishment projects next to Pearl Island (2021–2023), the nourished beaches experienced substantial accretion, while the unnourished beaches (H23–25) also experienced some accretion (Figures 12d and A6d).

4.6. Shoreline Changes before and after Beach Nourishments

The five beach nourishment projects significantly impacted the shoreline changes of the nourished beaches (H6–13, H19–22, and H26–34). Beach nourishment resulted in unusually rapid changes in shoreline position, making it necessary to use a smaller timeframe for analysis (Figures 13 and 14).

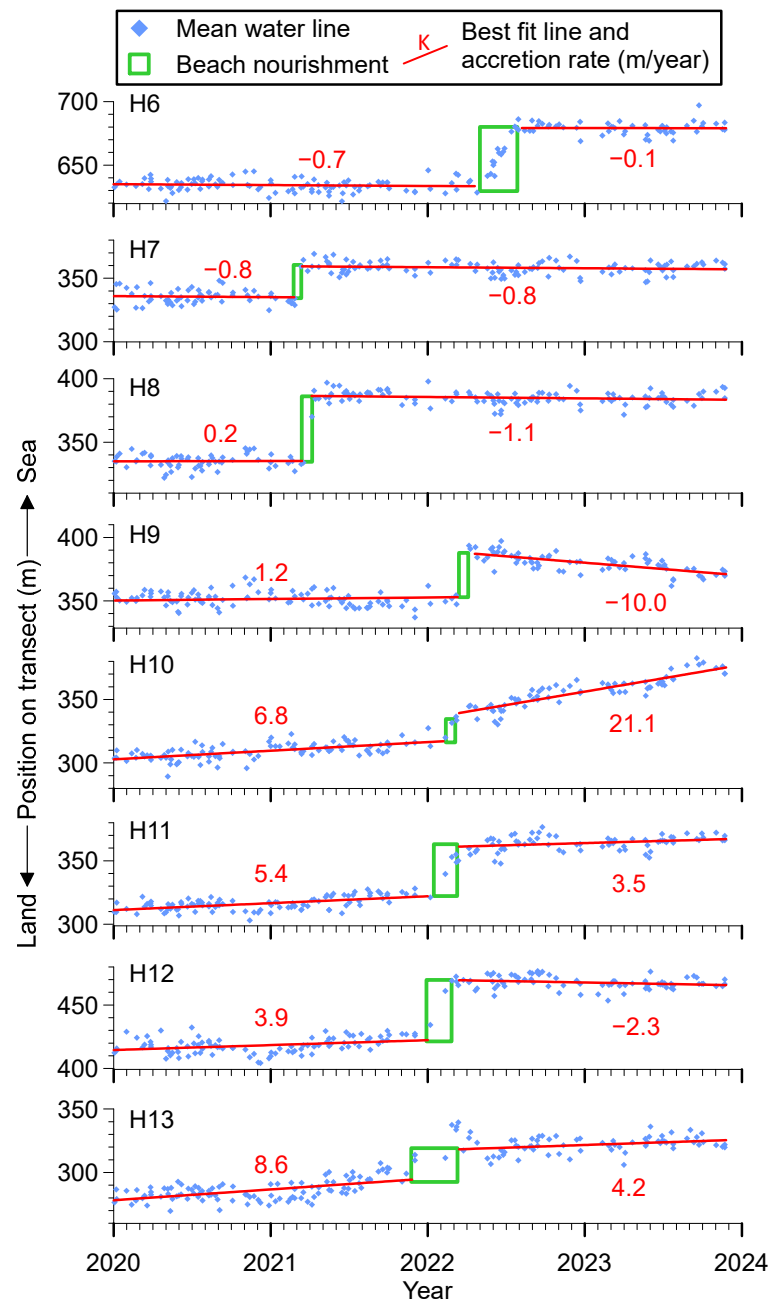


Figure 13. Satellite-derived positions of mean water line on transects H6–13 before and after beach nourishments. The green rectangle's dimensions indicate the duration of beach nourishment and the immediate beach width increment.

The beach nourishment projects were generally completed within a short period. For instance, the beach nourishment at transects H7–9 and H26–27 took less than a week. Even in the 2020s, when satellite images were captured approximately every 5 days, no images of nourishing beaches were obtained, resulting in a step-like signal in the shoreline position sequence. Some beaches experienced longer nourishing periods, such as transects H6, H11, and H20–21, lasting about 3 months. Multiple satellite images captured the gradual seaward shoreline movement process. The beach nourishments at transects H28 and H31 lasted even longer (about 4–5 months), and the shoreline position changes were more complex.

After beach nourishment projects were completed, rapid shoreline erosion generally occurred. However, there were exceptions, such as transect H10, which experienced rapid

accretion, with an accretion rate of 21.1 m/year. This study compared the shoreline change rates before and after beach nourishment and found a strong correlation between the two (Figure 15a). The study also compared the shoreline change rates after beach nourishment with the beach width increments caused by beach nourishment and similarly found a strong correlation between the two (Figure 15b).

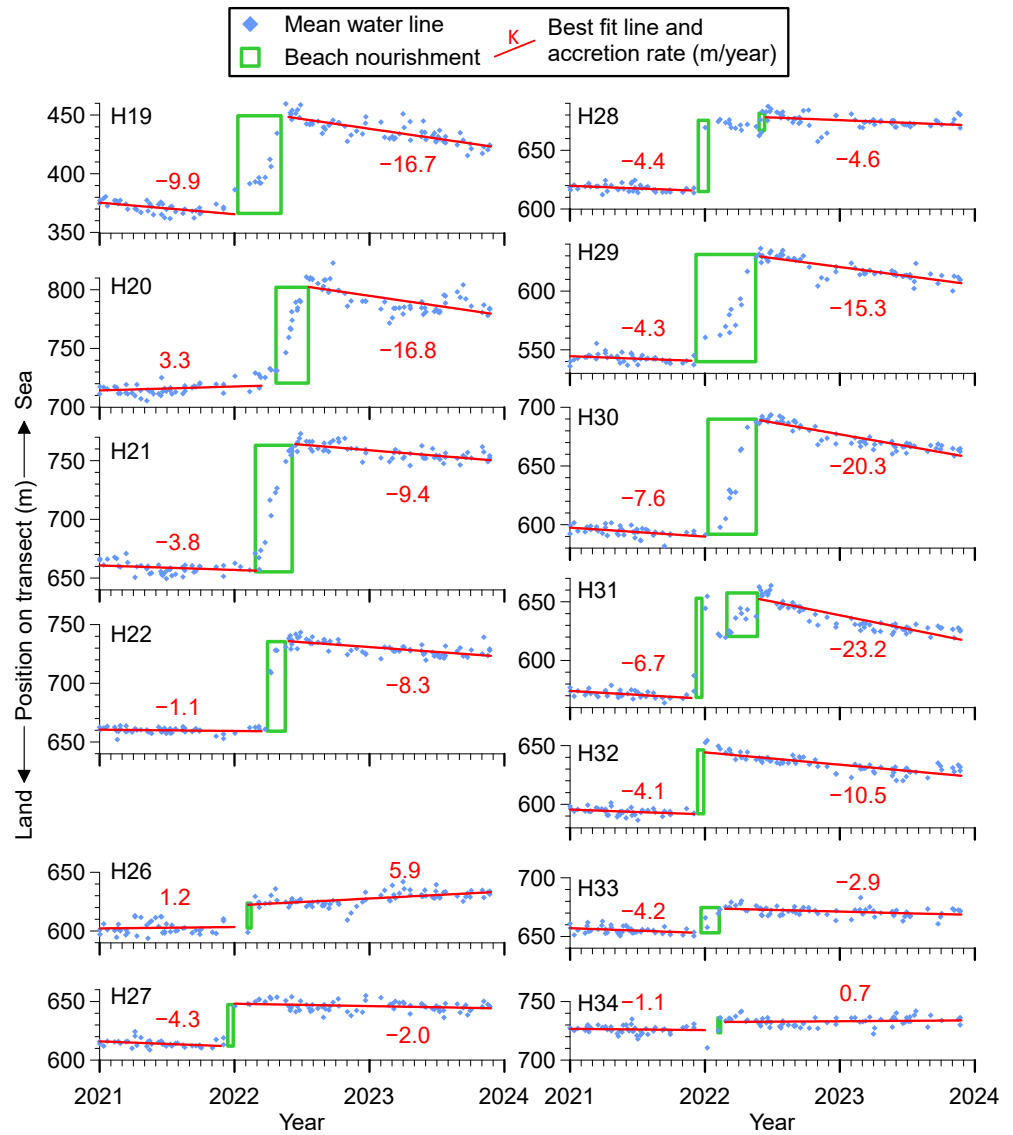


Figure 14. Satellite-derived positions of mean water line on transects H19–34 before and after beach nourishments.

A binary regression analysis was conducted to derive an equation (Equation (2)) that can be used to predict the shoreline change rate after beach nourishment based on the shoreline change rate before nourishment and the beach width increment due to nourishment.

$$SCR_{after} = 0.80 \times SCR_{before} - 0.20 \times BWI + 6.59 \tag{2}$$

where SCR_{before} and SCR_{after} represent the shoreline change rates before and after beach nourishment, respectively, and BWI indicates the beach width increment due to beach nourishment.

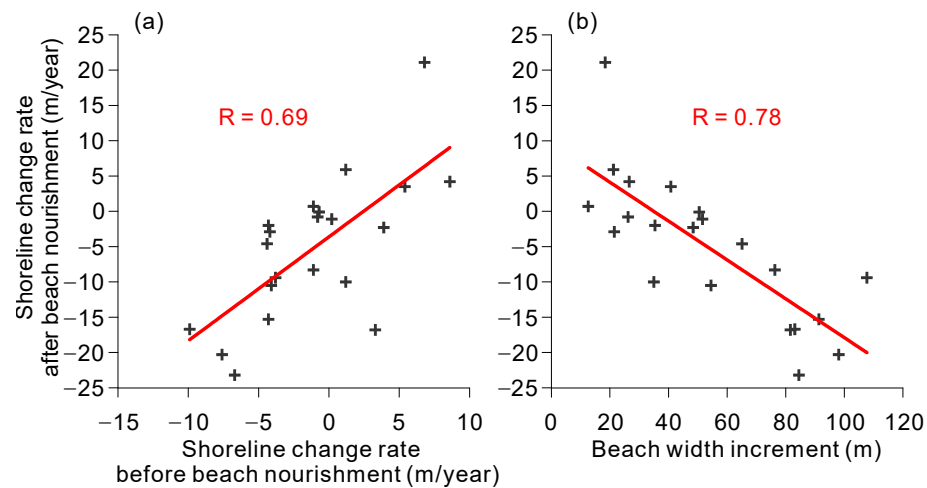


Figure 15. Relationship between shoreline change rates before and after beach nourishments (a); relationship between shoreline change rates after beach nourishments and beach width increments (b).

5. Discussion

5.1. Shoreline Change Characteristics and Main Influencing Factors

The shoreline changes at Haikou Beach exhibit phased and linear characteristics, with most erosion and accretion transitions clearly associated with coastal engineering construction. As mentioned earlier, the shoreline changes of Haikou Beach can be divided into three periods: 1986–2010, 2010–2020, and 2020–2023.

During the early period of 1986–2010, there were relatively few coastal engineering projects, and Haikou Beach was primarily undergoing natural and mild changes. The beaches near capes experienced accretion, while erosion occurred between capes (Figure 11a). This indicates that the beaches were transitioning from straight beaches to pocket beaches, with the western beaches (H1–13) beginning to exhibit pocket beach formation, while the eastern beaches (H14–37) remained relatively straight. The occasional transitions between erosion and accretion during this period could be linked to specific coastal engineering constructions, such as the construction of Trestle, where its western beach (transect H7) transitioned from accretion to erosion, while its eastern beach (H8–10) experienced accelerated erosion. The shoreline changes during this period are in general agreement with previous study [10], but our results are more detailed and spatially extensive.

During the middle period of 2010–2020, the extensive implementation of coastal engineering projects significantly altered the evolution of Haikou Beach, primarily leading to beach accretion around the engineering structures (Figure 11b). For instance, the construction of Groin 1 accelerated the accretion of transects H1–3; the construction of Millennium Island caused transects H8–10 to transition from erosion to accretion and slowed down the erosion of H11–12 (Figure 8). The construction of Pearl Island exerted a more significant influence on the evolution of its surrounding beaches (Figures 9 and 10), which will be discussed in the next section. The effects of engineering projects built before 2010 also persisted, such as the impact of Trestle on transects H7–10. The influence of Groin 2, constructed in 2008, began to manifest, leading to the transition from accretion to erosion for transect H14 in 2010 (Figure 8).

The coastal projects mentioned above, including Pearl Island, not only directly contributed to the accretion of their neighboring beaches but also primarily contributed to the erosion of their eastern beaches after 1–4 years (Figures 8–10). However, the coastal projects located to the east of Haikou Beach, such as Sailing Port, Xiuying Port, and Gourd Island, did not produce observable effects on Haikou Beach (Figure 10). Based on these observations, we speculate that sediment transport near Haikou Beach is predominantly from west to east. Coastal engineering projects not only directly affect (mainly weakening)

the hydrodynamic environment of the surrounding area, thereby influencing (mainly promoting accretion) the evolution of their neighboring beaches, but also hinder the transport of sediment from west to east, slowing down accretion or causing erosion on their eastern beaches. The changes in this period are basically consistent with previous study [11], but our results have a greater spatial and temporal range and resolution.

During the late period of 2020–2023, the shoreline changes were mainly dominated by beach nourishments (Figure 11c). Beach nourishment led to a rapid seaward movement of the shoreline, followed by a significant retreat (Figures 13 and 14). The results were even able to depict the detailed process of the five beach nourishment events (Figures 13 and 14), which had not been reported before.

In summary, the phased and linear characteristics of the shoreline changes, as well as the clear associations with coastal engineering projects, highlight the dominant role of human interventions in shaping the evolution of Haikou Beach. The main influencing factors include the construction of coastal engineering structures, the west-to-east sediment transport, and the implementation of beach nourishment projects. In addition, it should be pointed out that the interpretation of shoreline positions from satellite images with limited spatial resolution is inevitably constrained in precision. Therefore, it is necessary and feasible to fully leverage the large volume of available satellite images to extract as many shoreline positions as possible. By removing outliers through horizontal (spatial) and vertical (temporal) comparison between the interpretation results, and further improving the accuracy using statistical methods [28], the overall reliability of the research findings can be enhanced.

5.2. Influence of Offshore Artificial Islands Construction

The construction of Pearl Island has significantly impacted the evolution of Haikou Beach. Following the construction of Pearl Island Phase 1, the transects H19–25 experienced notable shoreline accretion (Figure 9). Specifically, transects H19–23 immediately accreted, while the eastern transects H24–25 began accreting within 1–2 years thereafter. The local waves are mainly from the NNE direction, and transects H19–25 happen to completely occupy the shadow zone of Pearl Island Phase 1 (between the red dashed lines in Figure 4b). Therefore, the accretion of transects H19–25 after the construction of Pearl Island Phase 1 can be attributed to the sheltering effect of the offshore artificial island.

The larger-scale Pearl Island Phase 2 has a larger shadow zone (H19–28, between the red dashed lines in Figure 4d). Following the construction of Phase 2, transects H23–25 within its shadow zone continued to accrete, while the eastern transects H26–28, also within its shadow zone but further east, began accreting after 1–2 years. However, the western transects H19–22 within its shadow zone experienced erosion for 3–5 years. Specifically, the erosion of transects H19–20 began immediately after the construction, while the erosion onset for the eastern transects H21–22 was delayed by 1–2 years, with a slightly reduced erosion rate but a longer duration.

Liu et al. [11] attributed the erosion of transects H19–22 as well as H14 to the change in wave direction caused by the construction of Pearl Island, which subsequently altered the sediment transport direction. We disagree with this viewpoint because this erosion of transects H19–22 only occurred within 3–5 years after the construction of Pearl Island Phase 2. If the mechanism were at play, then the area should have experienced erosion instead of actual accretion after the construction of Pearl Island Phase 1, and the erosion should not stop 3–5 years after the construction of Pearl Island Phase 2, when its eastern beach was still rapidly accreting. As for H14, the onset of erosion occurred prior to Pearl Island construction and should have little to do with the construction. Given that Pearl Island Phase 2 was larger in scale than Pearl Island Phase 1, its sheltering effect should have been stronger. If only the impact of Pearl Island Phase 2 were considered, transects H19–22 should have experienced accelerated accretion, or at least should not have turned to erosion. Therefore, this erosion must have had another cause.

We believe that the short-term erosion of transects H19–22 within 3–5 years after the construction of Pearl Island Phase 2 is due to nearshore sand mining. Nearshore sand mining has been reported to cause short-term and rapid erosion of neighboring beaches by Zhang et al. [25] at Haiyang Beach. Additionally, the high spatial-resolution satellite image on 24 August 2015 from Google Earth showed three ships in the northwest sea area of transects H19–22 (the red circle in Figure 4c), while no other satellite images from Google Earth have shown any ships in this sea area; therefore, we guess that these three boats were mining sand here at this time. This sand mining project also affected the beaches near transects H15–18, leading to a sudden shoreline retreat in 2015 (Figures 8 and 9).

Liu et al. [11] also attributed the erosion of the eastern beach (H31–33) to the construction of Pearl Island, stating that the construction altered the sediment transport direction, thereby causing the erosion. We agree that this erosion is related to the construction but disagree with this explanation. If the sediment transport direction had changed from eastward to westward, then the erosion of transects H31–33, located in the sediment source area, should not have occurred after the accretion of transects H19–23 in the sediment sink area. Additionally, the eastern transect H33 in sediment source area should have eroded before the western transect H31, yet the opposite is the fact.

We believe that this erosion should be attributed to the barrier effect of Pearl Island on sediment transport. The construction of Pearl Island facilitated sediment settling in its shadow zone, leading to erosion in the downstream (eastern) beach due to a lack of sediment supply. This erosion developed gradually from west to east (from H31 to H32) and was delayed by 2 years. Currently, the erosion in this area has slowed down, indicating that besides the barrier effect, the previous rapid erosion might also be contributed to neighboring sand mining during the construction of Pearl Island Phase 1.

The data used in Liu et al. [11] are mainly field measurements for 2010–2011 and 2019–2021, and the lack of data for 2012–2018, just after the construction of Pearl Island, may have affected the attribution analysis. The results obtained from long-term and continuous satellite images compensated for the shortcomings of field measurements in terms of spatiotemporal range and resolution, aiding in a more accurate analysis of the causes and mechanisms behind beach evolution.

The construction of Millennium Island has also resulted in the transition from erosion to accretion of the beach in its shadow area (H8–10) (Figures 8 and A1). The low accretion rate in this area compared to the shadow zone of Pearl Island may be due to the relative closure of the beach and the consequent lack of sediment sources. This interpretation is supported by the rapid accretion of transect H10 at a rate of 21.1 m/year after sand replenishment in 2022. The construction of Gourd Island did not cause observable changes in its surrounding shoreline, or more accurately, coastline, which can be attributed to the complete artificialization of its adjacent coast.

In summary, the construction of Pearl Island and Millennium Island resulted in significant accretion in their shadow beaches by blocking the incident waves, and the construction of Pearl Island further resulted in the erosion in its eastern beaches by blocking the alongshore sediment transport. The impact of large, offshore artificial islands on beach evolution differs from that of linear, nearshore detached breakwaters. The latter causes sediment on both sides to move toward the center of the shadow zone, resulting in erosion on both sides and accretion in the center.

5.3. Future Evolution of Haikou Beach and Measures for Its Management and Protection

The phased and linear shoreline changes of Haikou Beach, which are closely linked to human activities, provide favorable conditions for predicting its future evolution. In the future, the western beaches (H1–13), except those directly opposite Millennium Island, will continue to develop into pocket beaches. The beach evolution adjacent to Millennium Island was interrupted by the construction of the island. In the future, the beaches directly opposite Millennium Island will remain stable or even accrete, while its eastern beach will continue to develop into a pocket beach.

The construction of Pearl Island has divided the eastern Haikou Beach into three parts: western (H14–18), central (H19–28), and eastern (H29–37). The western part will receive sediment transported from the west and the sediment discharged by the Wuyuan River, and will maintain stability or even accrete. The eastern part, however, will experience erosion due to the barrier effect of Pearl Island. Given the considerable length of this part, continuous erosion and the formation of a pocket beach will result in significant erosion, adversely affecting nearby urban roads and buildings. Moderate sand replenishment should be considered for this part in the future to address these issues. The central part facing Pearl Island will continue to accrete under the island’s shelter.

Managers and engineers are particularly concerned about the formation of tombolo or salient on beaches facing offshore hard structures, as tombolo can completely block littoral sediment transport and have a greater detrimental impact on downstream beaches. Due to the relatively limited number of completed offshore artificial islands, relevant research is mainly conducted with reference to studies on detached breakwaters, and the main variables under consideration are the ratio (D/L) between the offshore distance (D) and the obstacle length (L) [35–37], or its reciprocal (L/D) [38]. The authors reviewed previous empirical formulas to assess the likelihood of tombolo or salient formation in front of Pearl Island (Table 3).

Table 3. Prediction of whether a salient or tombolo will be formed on beaches facing offshore artificial islands.

| | Millennium Island | Pearl Island Phase 1 | Pearl Island Phase 2 | Gourd Island |
|---|-------------------|----------------------|----------------------|--------------|
| Obstacle length (L) (m) | 340 | 1655 | 2300 | 1038 |
| Offshore distance (D) (m) | 250 | 2763 | 1850 | 423 |
| D/L | 0.735 | 1.669 | 0.804 | 0.408 |
| L/D | 1.360 | 0.599 | 1.243 | 2.454 |
| Tombolo or salient according to [35] | Tombolo | Tombolo | Tombolo | Tombolo |
| Tombolo or salient according to [36] | Tombolo | Salient | Tombolo | Tombolo |
| Tombolo or salient according to [37] | Tombolo | Salient | 50/50 chance | Tombolo |
| Tombolo or salient according to [38] | Tombolo | / | Tombolo | Tombolo |
| Predicted salient amplitude (m) according to [39] | 158 | 2081 | 1191 | 235 |
| Predicted salient amplitude (m) according to [40] | 85 | 1443 | 661 | 106 |
| Predicted salient amplitude (m) according to [41] | 138 | 1271 | 1005 | 258 |
| Average of predicted salient amplitude (m) | 127 | 1598 | 953 | 200 |
| Maximum shoreline change rate (m/year) | 1.5 | 7.3 | 7.3 | 0 |
| Time to beach equilibrium (year) | 85 | 219 | 130 | / |

According to Chen et al. [35], when the D/L is less than 2, a tombolo will form; and when the D/L is greater than 8.0, the beach will not be affected; thus, a tombolo will form. According to Dally et al. [36], when the ratio D/L is 0.5–0.67, a tombolo will form; and when the ratio D/L is 1.5–2, a salient will form. The D/L ratio of Pearl Island Phase 2 is 0.804, thus, there is a greater likelihood of a tombolo forming according to Dally et al. [36]. According to [37], a tombolo will form when the ratio D/L is less than 0.8, and a salient will form when the ratio D/L is greater than 0.8; thus, there is a 50/50 chance of forming tombolo or salient. According to Suh et al. [38], a tombolo will form when the ratio L/D is greater than 1; the L/D ratio of Pearl Island Phase 2 is 1.243, thus, a tombolo will form.

According to the existing formulas, there is a high likelihood of a tombolo forming in front of Pearl Island. However, it is important to note that these empirical formulas deduced from linear, nearshore detached breakwaters may not be directly applicable to the large, offshore artificial island of Pearl Island. Suh et al. [38], Ming and Chiew [37], and Chen et al. [35] are based on the laboratory results of detached breakwaters located at offshore distances of 0.3–0.5, 0.6–1.5, and 11.8–21.3 m, respectively. Dally [36] studied field detached breakwaters at offshore distances ranging from 46–600 m. However, the offshore distance of Pearl Island is 1850 m, far exceeding the above distances. Additionally, other factors such as waves, tides, water depth, beach slope, and sediment supply can also influence the beach changes [35–37], making it difficult to accurately predict the formation of a tombolo or salient.

If a tombolo forms at the current fastest accretion rate (7.3 m/year), it would take 253 years. If a salient forms, according to the formulas by Hsu and Silvester [39], Black and Andrews [40], and Sulis et al. [41], the predicted salient amplitude is 1191, 661, and 1005 m, averaging 953 m; it would take 130 years to reach beach equilibrium at the current fastest accretion rate. These results indicate that whether a tombolo or salient forms, the process will be lengthy. Furthermore, considering the crucial role of sufficient sediment supply in determining the formation of a salient or tombolo, reducing or eliminating sand replenishment on the western beaches of Pearl Island should be considered to delay this process.

To manage and protect Haikou Beach, the authors suggest considering the following measures: (1) moderate sand replenishment for the eastern beaches (H29–37) to address the erosion caused by the barrier effect of Pearl Island; (2) reducing or eliminating sand replenishment on the western beaches of Pearl Island to delay the potential formation of a tombolo or salient, as sufficient sediment supply is a crucial factor.

The future evolution of Haikou Beach will continue to be shaped by the complex interplay between natural processes and human interventions, requiring careful monitoring and adaptive management strategies to ensure the long-term sustainability of the coastal environment.

6. Conclusions

This study shows that the extensive use of satellite images and sub-pixel shoreline identification techniques overcame the limitations of insufficient spatial resolution in public satellite images, significantly improving the accuracy and temporal resolution of shoreline positions. This led to detailed and reliable beach evolution processes, addressing the common limitations of ground survey data in terms of spatiotemporal range and resolution.

The identification feature of waterline on the satellite images of Haikou Beach is evident, and the steep intertidal slope makes the waterline position less affected by tidal fluctuation. Apart from the beaches near the estuary, the random error in the waterline position averaged 7.9 m. After georeferencing and water level corrections, the random error averaged 4.9 m, ranking among the state-of-the-art studies.

The shoreline positions of Haikou Beach exhibit phased and linear changes over time, with most erosion and accretion transitions clearly associated with adjacent coastal engineering construction. The construction of artificial offshore islands, including Pearl Island and Millennium Island, exerted a predominantly positive impact on the evolution of Haikou Beach, leading to rapid accretion in their shadow areas. However, Pearl Island also obstructed sediment transport from west to east, resulting in minor erosion on its southeast beach. This study does not support the occurrence of erosion on the sediment source side of large, offshore artificial islands, which differs from the impact of linear, nearshore breakwaters.

Beach nourishments significantly impacted the evolution of Haikou Beach, leading to rapid accretion and subsequent erosion. The post-nourishment beach erosion rate can be estimated using the pre-nourishment shoreline change rate and the beach width increment due to the nourishment project.

In the future, the western beaches will continue to develop towards pocket beaches, while the straight eastern beaches will be divided into three parts due to the construction of Pearl Island. The western part will maintain stability or experience accretion, while the eastern part will suffer erosion due to the barrier effect of Pearl Island, requiring appropriate sand replenishment. The beach in the wave shadow area of Pearl Island may form a tombolo or a huge salient, but this formation may take over a hundred years, and reducing or eliminating sand replenishment on the western part of Pearl Island could delay this process.

Under the current backdrop of global changes and heightened human activities, a meticulous examination of the historical evolution of urban beaches and their correlation with coastal engineering construction is not only crucial for environmental impact assessment in coastal engineering but also contributes to a deeper comprehension of the causes and mechanisms behind beach evolution. Existing satellite imagery has already demonstrated its superiority in studying the evolution of beaches. With the continued advancement of remote sensing technology, an increasing number of higher-quality satellite images will become available in the future. In conclusion, the application of remote sensing methods to investigate the evolution of urban beaches holds great promise for the future.

Author Contributions: Conceptualization, R.H. and X.Z.; methodology, X.Z.; software, X.Z.; validation, Y.F.; formal analysis, Y.F.; investigation, Y.F.; resources, R.H. and X.Z.; data curation, R.H. and X.Z.; writing—original draft preparation, R.H. and X.Z.; writing—review and editing, Y.F. and X.Z.; visualization, Y.F. and X.Z.; supervision, X.Z.; project administration, X.Z.; funding acquisition, R.H. and X.Z. All authors have read and agreed to the published version of the manuscript.

Funding: This research was funded by the National Natural Science Foundation of China (42276172) and the Tung International Research Center for Sustainable Ocean Development.

Data Availability Statement: The CASPRS software, GEE downloader 2.0 program, and sample data can be downloaded from Figshare (<https://doi.org/10.6084/m9.figshare.23731110>, accessed on 1 January 2024); the satellite images can be downloaded from GEE (<https://earthengine.google.com/>).

Conflicts of Interest: The authors declare no conflicts of interest.

Appendix A

Appendix A includes following six figures: Figure A1. Building process of Trestle, Groin 2, Millennium Island, and Groin 1; Figure A2. Building process of Sailing Port, Xiuying Port, and Gourd Island; Figure A3. Beach nourishments at transects H6–13 from 2021 to 2022; Figure A4. Beach nourishments at transects H19–22 and H26–34 in 2022; Figure A5. Shoreline movements of Haikou beach during 1989–2010 (a), 2010–2020 (b), 2020–2023 (c), and 1989–2023 (d); Figure A6. Shoreline movements of Haikou beach next to Pearl Island during 2001–2011 (a), 2011–2015 (b), 2015–2021 (c), and 2021–2023 (d).

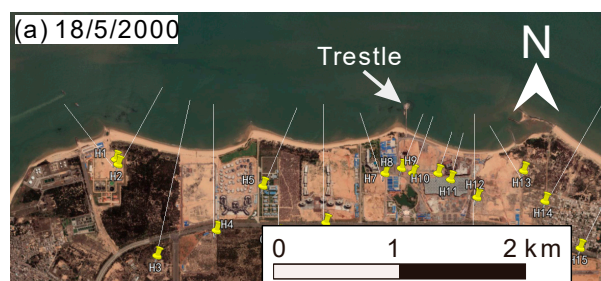


Figure A1. Cont.

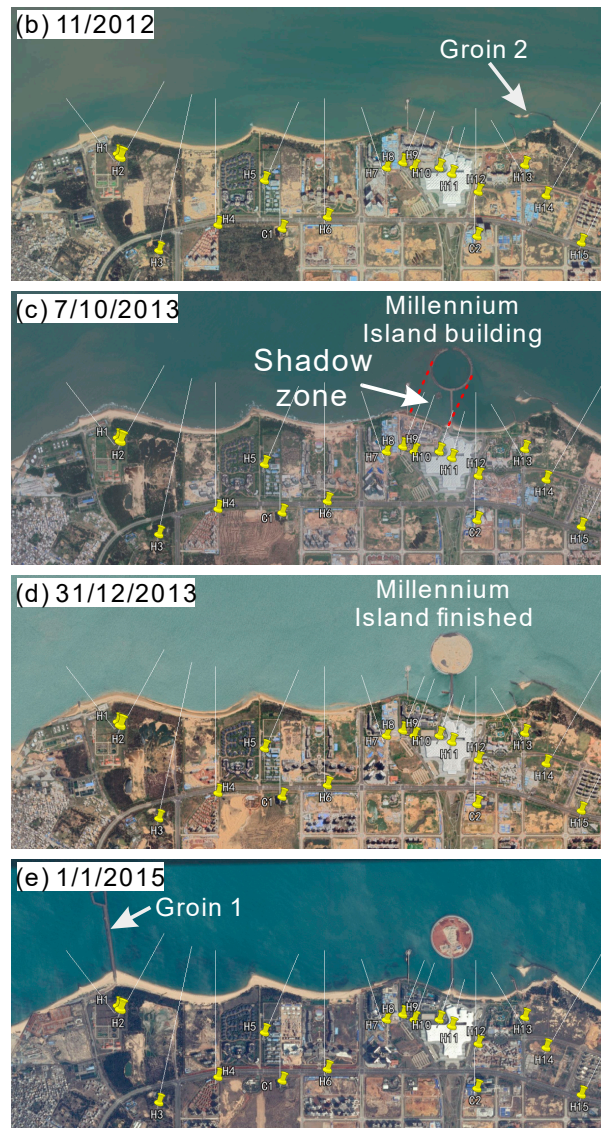


Figure A1. Building process of Trestle, Groin 2, Millennium Island, and Groin 1. Background images are from Google Earth.



Figure A2. Cont.



Figure A2. Building process of Sailing Port, Xiuying Port, and Gourd Island. Background images are from Google Earth.

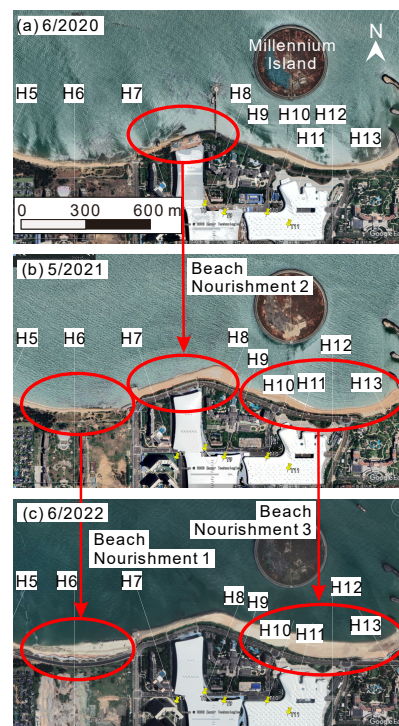


Figure A3. Beach nourishments at transects H6–H13 from 2021 to 2022. (a) Before Beach Nourishment 2, (b) immediately after Beach nourishment 2 and before Beach Nourishment 1, and (c) immediately after Beach Nourishment 1. Background images are from Google Earth.

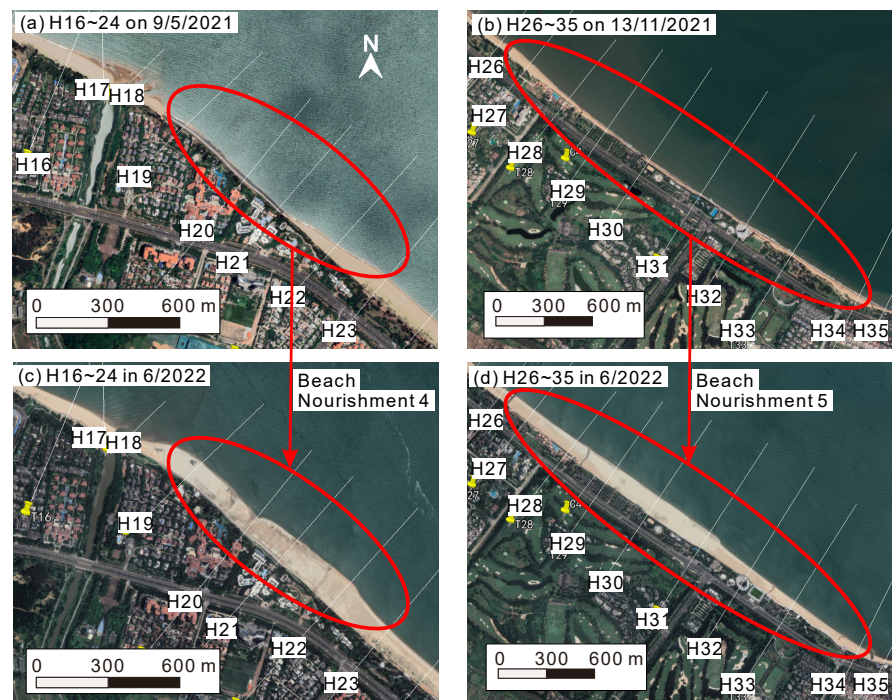


Figure A4. Beach nourishments at transects H19–22 and H26–34 in 2022. (a) The beach around transects H16–24 before Beach Nourishment 4, (b) the beach around transects H26–34 before Beach Nourishment 5, (c) the beach around transects H16–24 immediately after Beach Nourishment 4, and (d) the beach around transects H26–34 immediately after Beach Nourishment 5. Background images are from Google Earth.

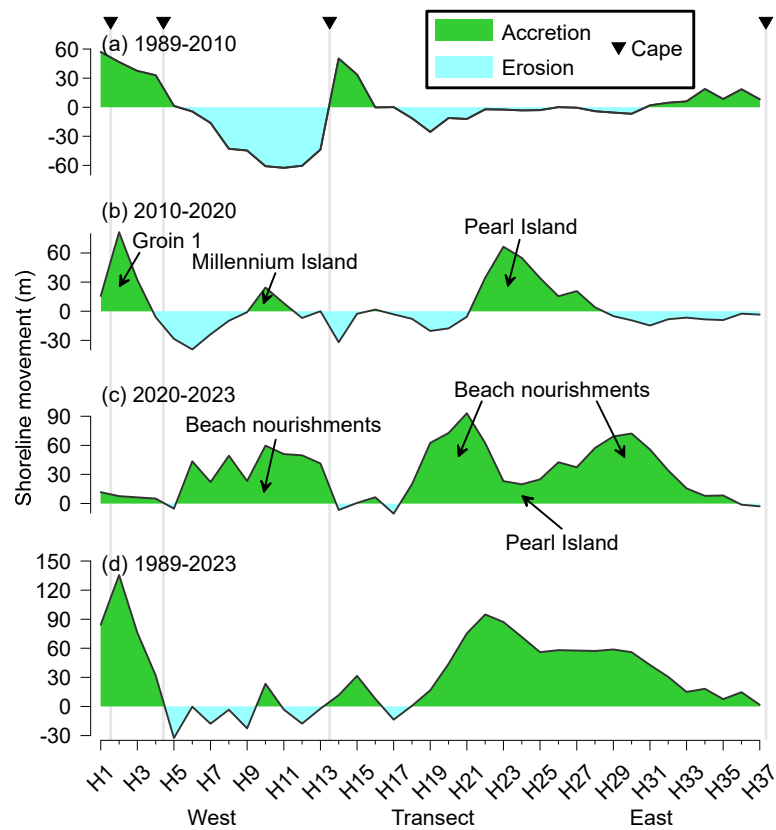


Figure A5. Shoreline movements of Haikou beach during 1989–2010 (a), 2010–2020 (b), 2020–2023 (c), and 1989–2023 (d).

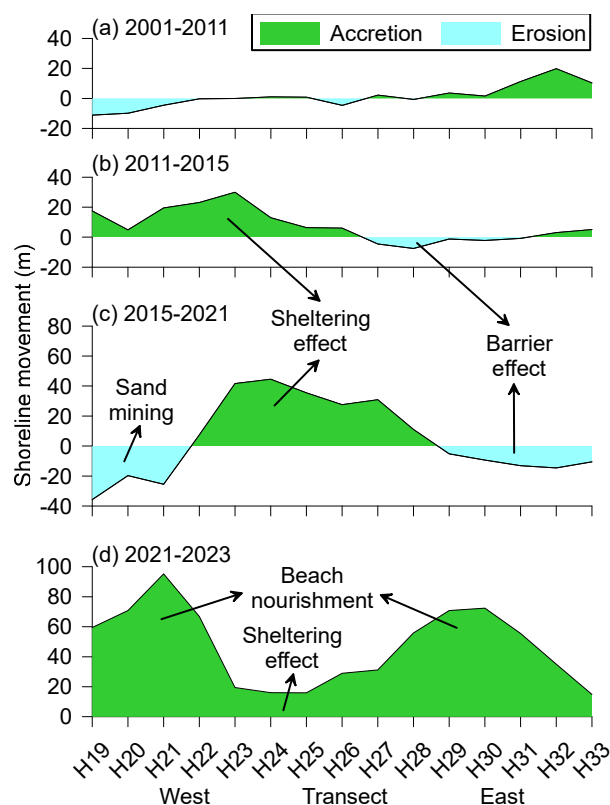


Figure A6. Shoreline movements of Haikou beach next to Pearl Island during 2001–2011 (a), 2011–2015 (b), 2015–2021 (c), and 2021–2023 (d).

References

- de Schipper, M.A.; Ludka, B.C.; Raubenheimer, B.; Luijendijk, A.P.; Schlacher, T.A. Beach nourishment has complex implications for the future of sandy shores. *Nat. Rev. Earth Environ.* **2021**, *2*, 70–84. [\[CrossRef\]](#)
- Turner, I.L.; Harley, M.D.; Almar, R.; Bergsma, E.W.J. Satellite optical imagery in Coastal Engineering. *Coast. Eng.* **2021**, *167*, 103919. [\[CrossRef\]](#)
- Hulskamp, R.; Luijendijk, A.; van Maren, B.; Moreno-Rodenas, A.; Calkoen, F.; Kras, E.; Lhermitte, S.; Aarninkhof, S. Global distribution and dynamics of muddy coasts. *Nat. Commun.* **2023**, *14*, 8259. [\[CrossRef\]](#) [\[PubMed\]](#)
- Armstrong, S.B.; Lazarus, E.D. Masked shoreline erosion at large spatial scales as a collective effect of beach nourishment. *Earth's Future* **2019**, *7*, 74–84. [\[CrossRef\]](#)
- Jackson, N.L.; Nordstrom, K.F. Trends in research on beaches and dunes on sandy shores, 1969–2019. *Geomorphology* **2020**, *366*, 106737. [\[CrossRef\]](#)
- Li, S.; Lv, B.; Yang, Y.; Wang, C. Effects of offshore artificial islands on beach stability of sandy shores: Case study of Hongtang Bay, Hainan Province. *Front. Earth Sci.* **2022**, *16*, 876–889. [\[CrossRef\]](#)
- Turner, I.L.; Harley, M.D.; Short, A.D.; Simmons, J.A.; Bracs, M.A.; Phillips, M.S.; Splinter, K.D. A multi-decade dataset of monthly beach profile surveys and inshore wave forcing at Narrabeen, Australia. *Sci. Data* **2016**, *3*, 160024. [\[CrossRef\]](#) [\[PubMed\]](#)
- Castelle, B.; Bujan, S.; Marieu, V.; Ferreira, S. 16 years of topographic surveys of rip-channelled high-energy meso-macrotidal sandy beach. *Sci. Data* **2020**, *7*, 410. [\[CrossRef\]](#) [\[PubMed\]](#)
- Vandenhove, M.; Castelle, B.; Lerma, A.N.; Marieu, V.; Dalet, E.; Hanquiez, V.; Mazeiraud, V.; Bujan, S.; Mallet, C. Secular shoreline response to large-scale estuarine shoal migration and welding. *Geomorphology* **2024**, *445*, 108972. [\[CrossRef\]](#)
- Zhou, H.Y. Sedimentary Characteristic and Topographical Evolution of Haikou Bay, Gaolong Bay and Boao Beaches in Hainan. Master's Thesis, East China Normal University, Shanghai, China, 2013; p. 80, (In Chinese with English Abstract).
- Liu, G.; Qi, H.; Cai, F.; Zhu, J.; Zhao, S.; Liu, J.; Lei, G.; Cao, C.; He, Y.; Xiao, Z. Initial morphological responses of coastal beaches to a mega offshore artificial island. *Earth Surf. Process. Landf.* **2022**, *47*, 1355–1370. [\[CrossRef\]](#)
- Luijendijk, A.; Hagenaars, G.; Ranasinghe, R.; Baart, F.; Donchyts, G.; Aarninkhof, S. The State of the World's Beaches. *Sci. Rep.* **2018**, *8*, 6641. [\[CrossRef\]](#)

13. Vousdoukas, M.I.; Ranasinghe, R.; Mentaschi, L.; Plomaritis, T.A.; Athanasiou, P.; Luijendijk, A.; Feyen, L. Sandy coastlines under threat of erosion. *Nat. Clim. Change* **2020**, *10*, 260–263. [[CrossRef](#)]
14. Ding, Y.; Yang, X.; Jin, H.; Wang, Z.; Liu, Y.; Liu, B.; Zhang, J.; Liu, X.; Gao, K.; Meng, D. Monitoring Coastline Changes of the Malay Islands Based on Google Earth Engine and Dense Time-Series Remote Sensing Images. *Remote Sens.* **2021**, *13*, 3842. [[CrossRef](#)]
15. Chi, S.; Zhang, C.; Wang, P.; Shi, J.; Li, F.; Li, Y.; Wang, P.; Zheng, J.; Sun, J.; Nguyen, V.T. Morphological evolution of paired sand spits at the Fudu river mouth: Wave effects and anthropogenic factors. *Mar. Geol.* **2023**, *456*, 106991. [[CrossRef](#)]
16. Murray, N.J.; Phinn, S.R.; Dewitt, M.; Ferrari, R.; Johnston, R.; Lyons, M.B.; Clinton, N.; Thau, D.; Fuller, R.A. The global distribution and trajectory of tidal flats. *Nature* **2019**, *565*, 222–225. [[CrossRef](#)]
17. Pardo-Pascual, J.; Almonacid-Caballer, J.; Ruiz, L.; Palomar-Vázquez, J. Automatic extraction of shorelines from Landsat TM and ETM+ multi-temporal images with subpixel precision. *Remote Sens. Environ.* **2012**, *123*, 1–11. [[CrossRef](#)]
18. Pardo-Pascual, J.E.; Sánchez-García, E.; Almonacid-Caballer, J.; Palomar-Vázquez, J.M.; de los Santos, E.P.; Fernández-Sarriá, A.; Balaguer-Beser, A. Assessing the accuracy of automatically extracted shorelines on microtidal beaches from Landsat 7, Landsat 8 and Sentinel-2 imagery. *Remote Sens.* **2018**, *10*, 326. [[CrossRef](#)]
19. Pardo-Pascual, J.E.; Almonacid-Caballer, J.; Cabezas-Rabadán, C.; Fernández-Sarriá, A.; Armario, C.; Ciavola, P.; Montes, J.; Souto-Ceccon, P.E.; Palomar-Vázquez, J. Assessment of satellite-derived shorelines automatically extracted from Sentinel-2 imagery using SAET. *Coast. Eng.* **2024**, *188*, 104426. [[CrossRef](#)]
20. Hagenars, G.; de Vries, S.; Luijendijk, A.P.; de Boer, W.P.; Reniers, A.J.H.M. On the accuracy of automated shoreline detection derived from satellite imagery: A case study of the sand motor mega-scale nourishment. *Coast. Eng.* **2018**, *133*, 113–125. [[CrossRef](#)]
21. Vos, K.; Harley, M.D.; Splinter, K.D.; Simmons, J.A.; Turner, I.L. Sub-annual to multi-decadal shoreline variability from publicly available satellite imagery. *Coast. Eng.* **2019**, *150*, 160–174. [[CrossRef](#)]
22. Vos, K.; Splinter, K.D.; Palomar-Vázquez, J.; Pardo-Pascual, J.E.; Almonacid-Caballer, J.; Cabezas-Rabadán, C.; Kras, E.C.; Luijendijk, A.P.; Calkoen, F.; Almeida, L.P.; et al. Benchmarking satellite-derived shoreline mapping algorithms. *Commun. Earth Environ.* **2023**, *4*, 345. [[CrossRef](#)]
23. Castelle, B.; Masselink, G.; Scott, T.; Stokes, C.; Konstantinou, A.; Marieu, V.; Bujan, S. Satellite-derived shoreline detection at a high-energy meso-macrotidal beach. *Geomorphology* **2021**, *383*, 107707. [[CrossRef](#)]
24. Zhang, X.D.; Yang, Z.S.; Zhang, Y.X.; Ji, Y.; Wang, H.M.; Lv, K.; Lu, Z.Y. Spatial and temporal shoreline changes of the southern Yellow River (Huanghe) Delta in 1976–2016. *Mar. Geol.* **2018**, *395*, 188–197. [[CrossRef](#)]
25. Zhang, X.D.; Tan, X.W.; Hu, R.J.; Zhu, L.H.; Wu, C.; Yang, Z.S. Using a transect-focused approach to interpret satellite images and analyze shoreline evolution in Haiyang Beach, China. *Mar. Geol.* **2021**, *438*, 106526. [[CrossRef](#)]
26. Zhang, X.D.; Wu, C.; Zhang, Y.C.; Hu, R.J.; Yang, Z.S. Using free satellite imagery to study the long-term evolution of intertidal bar systems. *Coast. Eng.* **2022**, *174*, 104123. [[CrossRef](#)]
27. Zhang, X.D.; Yao, Y.H.; Zhu, L.H.; Hu, R.J.; Wu, C. Topographic and geomorphological evolution of Huiquan Beach of Qingdao in past 40 years using massive satellite images. *Oceanol. Et. Limnol. Sin.* **2022**, *53*, 578–589, (In Chinese with English Abstract).
28. Zhang, X.D.; Wu, C.; Hu, R.J.; Xu, S.M.; Xu, Z.R.; Yang, Z.S. Can Satellite-derived Beach Images Resolve the Responses to Human Activities? *J. Geophys. Res. Earth Surf.* **2024**, *129*, e2023JF007339. [[CrossRef](#)]
29. Zhang, X.D. Computer-aided shoreline position recognition software [Software]. *Figshare* **2023**. Available online: <https://figshare.com/articles/software/CASPRS/23731110> (accessed on 18 January 2024).
30. Subrauel, P.; Ebraheem, A.A.; Sherif, M.; Sefelnasr, A.; Yagoub, M.M.; Rao, K.N. Land in Water: The Study of Land Reclamation and Artificial Islands Formation in the UAE Coastal Zone: A Remote Sensing and GIS Perspective. *Land.* **2022**, *11*, 2024. [[CrossRef](#)]
31. Wang, C.F. Balancing Marine Development and Conservation Hainan Builds Ecological Barrier. *Economic Information Daily.* **2023**. Available online: http://www.jjckb.cn/2023-06/20/c_1310728683.htm (accessed on 20 June 2023).
32. Chen, S.L.; Gong, W.P.; Wang, B.C. Longshore sediment transport and nearshore evolution response for the Nanduijiang Delta, Hainan island. *Trans. Oceanol. Limnol.* **1998**, *1*, 23–32, (In Chinese with English Abstract).
33. Gorelick, N.; Hancher, M.; Dixon, M.; Ilyushchenko, S.; Thau, D.; Moore, R. Google Earth Engine: Planetary-scale geospatial analysis for everyone. *Remote Sens. Environ.* **2017**, *202*, 18–27. [[CrossRef](#)]
34. Matsumoto, K.; Takanezawa, T.; Ooe, M. Ocean tide model developed by assimilating TOPEX/POSEIDON altimetry data into hydrodynamical model: A global and a regional model around Japan. *J. Oceanogr.* **2000**, *56*, 567–581. [[CrossRef](#)]
35. Chen, Z.; Xu, M.; Lin, B. Some laws of tombolo formation and their application in harbour construction. *Acta Oceanol. Sin.* **1986**, *5*, 134–146.
36. Dally, W.R.; Pope, J. *Detached Breakwaters for Shore Protection*; Technical Report CERC-86-1; USACOE: Washington, DC, USA, 1986.
37. Ming, D.; Chiew, Y. Shoreline changes behind detached breakwater. *J. Waterw. Port. Coast. Ocean. Eng.* **2000**, *126*, 63–70. [[CrossRef](#)]
38. Suh, K.; Dalrymple, R.A. Offshore breakwaters in laboratory and field. *J. Waterw. Port. Coast. Ocean. Eng.* **1987**, *113*, 105–121. [[CrossRef](#)]
39. Hsu, J.R.; Silvester, R. Accretion behind single offshore breakwater. *J. Waterw. Port Coast. Ocean. Eng.* **1990**, *116*, 362–380. [[CrossRef](#)]

40. Black, K.P.; Andrews, C.J. Sandy shoreline response to offshore obstacles Part 1: Salient and tombolo geometry and shape. *J. Coast. Res. SI* **2001**, *29*, 82–93. Available online: <http://www.jstor.org/stable/25736207> (accessed on 18 January 2024).
41. Sulis, A.; Balzano, A.; Cabras, C.; Atzeni, A. On the applicability of empirical formulas for natural salients to Sardinia (Italy) beaches. *Geomorphology* **2017**, *286*, 1–13. [[CrossRef](#)]

Disclaimer/Publisher’s Note: The statements, opinions and data contained in all publications are solely those of the individual author(s) and contributor(s) and not of MDPI and/or the editor(s). MDPI and/or the editor(s) disclaim responsibility for any injury to people or property resulting from any ideas, methods, instructions or products referred to in the content.